Available online at www.sciencedirect.com
ScienceDirect
Journal of Sound and Vibration 305 (2007) 492–520
JOURNAL OF SOUND AND VIBRATION
www.elsevier.com/locate/jsvi

# Experiments and analysis on chaotic vibrations of a shallow cylindrical shell-panel

K. Nagai[a,*], S. Maruyama[a], T. Murata[b], T. Yamaguchi[a]

[a]*Department of Mechanical System Engineering, Gunma University, 1-5-1, Tenjin-cho, Kiryu, Gunma 376-8515, Japan*
[b]*Matsushita Refrigeration Company, 2-3-1-2, Noji-Higashi, Kusatsu, Shiga 525-8555, Japan*

Received 20 September 2006; received in revised form 5 February 2007; accepted 15 April 2007
Available online 27 June 2007

**Abstract**

Detailed experimental results and analytical results are presented on chaotic vibrations of a shallow cylindrical shell-panel subjected to gravity and periodic excitation. The shallow shell-panel with square boundary is simply supported for deflection. In-plane displacement at the boundary is elastically constrained by in-plain springs. In the experiment, the cylindrical shallow shell-panel with thickness 0.24 mm, square form of length 140 mm and mean radius 5150 mm is used for the test specimen. All edges around the shell boundary are simply supported by adhesive flexible films. First, to find fundamental properties of the shell-panel, linear natural frequencies and characteristics of restoring force of the shell-panel are measured. These results are compared with the relevant analytical results. Then, geometrical parameters of the shell-panel are identified. Exciting the shell-panel with lateral periodic acceleration, nonlinear frequency responses of the shell-panel are obtained by sweeping the frequency of periodic acceleration. In typical ranges of the exciting frequency, predominant chaotic responses are generated. Time histories of the responses are recorded for inspection of the chaos. In the analysis, the Donnell equation with lateral inertia force is introduced. Assuming mode functions, the governing equation is reduced to a set of nonlinear ordinary differential equations by the Galerkin procedure. Periodic responses are calculated by the harmonic balance method. Chaotic responses are integrated numerically by the Runge–Kutta–Gill method. The chaotic responses, which are obtained by the experiment and the analysis, are inspected with the Fourier spectra, the Poincaré projections, the maximum Lyapunov exponents and the Lyapunov dimension. It is found that the dominant chaotic responses of the shell-panel are generated from the responses of the sub-harmonic resonance of $\frac{1}{2}$ order and of the ultra-sub-harmonic resonance of $\frac{2}{3}$ order. By the convergence of the maximum Lyapunov exponent to the embedding dimension, the number of predominant vibration modes which contribute to the chaos is found to be three or four. Fairly good agreements are obtained between the experimental results and the analytical results.


## 1. Introduction

It is of practical importance and of academic interest to investigate chaotic vibrations of thin walled structures under periodic excitation. Shells and plates are fundamental elements of the structures and are

*Corresponding author. Tel.: +81 277 30 1584; fax: +81 277 30 1599.
*E-mail addresses:* nagai@eng.gunma-u.ac.jp (K. Nagai), maruyama@me.gunma-u.ac.jp (S. Maruyama), yamagme4@me.gunma-u.ac.jp (T. Yamaguchi).

0022-460X/$ - see front matter © 2007 Elsevier Ltd. All rights reserved.
doi:10.1016/j.jsv.2007.04.032

utilized practically in transport vehicles such as aircraft, spacecraft and others. Since the shell has curved configuration, lateral deflection of the shell is coupled to in-plane deformation intensely. Then, bending rigidity of the shell is increased than that of a plate. However, when lateral load on the shell exceeds ultimate magnitude, buckling phenomenon appears with the type of snap-through transition. Furthermore when the shell is excited by periodic load, nonlinear vibrations of the shell are generated with resonance. In typical regions of the exciting frequency, chaotic vibrations are generated with random-like responses involving dynamic snap-through transition, even though the amplitude of excitation is small. The generation of the chaotic response is drastically influenced by small fluctuations of configuration of the shell and constraint conditions at the boundary. In practical design of thin walled structures, it is important to predict occurrence of the chaotic phenomena precisely and also to stabilize the chaotic responses.

Nonlinear vibrations of shells have been investigated by many researchers. For nonlinear periodic responses of closed cylindrical shells, numbers of reports have been presented. To determine the characteristics of nonlinear frequency response curve, both analytical and experimental studies were conducted by Evensen for shells and rings [1,2] and by Olson for shells [3]. A cylindrical shell with both ends clamped was studied by Matsuzaki and Kobayashi [4], while Chen and Babcock [5] analyzed the nonlinear responses of a simply supported shell and conducted the experiment of shells with rings at both ends. Nonlinear response of a cantilevered cylindrical shell was studied experimentally by Chiba [6]. Pellicano et al. [7] and Amabili [8] presented a large amplitude periodic response of empty and fluid-filled circular cylindrical shells with simply supported ends. For shallow shell-panels, Kobayashi and Leissa [9] analyzed nonlinearity of free vibration. Experiment of nonlinear periodic responses of a cylindrical panel was conducted by Amabili et al. [10]. Aforementioned researches seem to have a focus on basic characteristics of the nonlinear periodic responses of the shells.

Chaotic phenomena of shells were investigated mainly for plates and shallow shells. Dowell [11] studied chaotic responses of an infinitely long buckled plate induced by an air flow. Nayfeh and Raouf [12] studied period-doubling bifurcations of nonlinear responses of an infinitely long cylindrical shell under the condition of internal resonance. For a square plate, Yang and Sethna [13] and Chang et al. [14] investigated nonlinear periodic responses and chaotic responses in the internal resonance condition. Fan et al. [15] analyzed chaotic responses of saddle form cable-suspended roofs by the Melnikov method. Popov et al. [16] analyzed chaotic energy exchange through auto-parametric resonance in cylindrical shells. Chaotic responses of a shallow spherical shell was studied by Soliman and Gonçalves [17]. Foregoing analyses were conducted under the assumption of relatively lower degree-of-freedom system. Amabili [18] analyzed nonlinear vibrations of doubly curved shallow shells and chaotic responses were calculated. Finite element approaches for shallow shells were conducted by Zhou et al. [19] and by Sansour et al. [20]. Experiments of dynamical responses of an aircraft panel and thermally buckled plates excited by acoustic pressure were conducted by Meastrello et al. [21] and by Murphy et al. [22], respectively.

The authors have investigated the nonlinear vibrations of a clamped arch [23,24] and chaotic vibrations of a post-buckled beam [25–27] both experimentally and analytically as fundamental studies of thin shells dynamics. In the studies, quantitative excellent agreements were obtained. The predominant chaotic responses are bifurcated from the sub-harmonic resonance responses of $\frac{1}{2}$ and $\frac{1}{3}$ orders. The authors also confirmed the same type of chaotic responses by the experiment of a post-buckled reinforced beam [28] and by the experiment of a clamped beam with axial elastic constraint [29]. For chaotic vibrations of shells, the authors have presented analytical results on chaotic responses of a shallow cylindrical shell-panel with simply supported rectangular boundary [30,31]. The analysis with multiple-degree-of-freedom system on the shell-panel is introduced. Under the various curvatures of the shell-panel, modal contribution to the chaotic responses was clarified [30]. Chaotic responses were also examined for shell-panel with in-plane elastic constraint at the boundary [31]. Furthermore, chaotic responses of the cylindrical shell-panel with a concentrated mass were analyzed [32]. Owing to the existence of the concentrated mass on the shell-panel, the contribution of vibration modes to the chaotic responses and the Lyapunov dimension are decreased. For the studies on chaotic vibrations of a shallow cylindrical shell-panel, it seems to the authors that experimental studies associated with analyses have not been presented.

The chaotic phenomena are very sensitive to the shell geometry and the boundary conditions. To reveal profound features of chaotic phenomena of a shallow cylindrical shell-panel, it is required that experimental

results and the relevant analytical results are verified complementarily with each other. In this paper, both experimental and analytical results are presented. The shallow cylindrical shell-panel is simply supported for deflection at a square boundary. The shell-panel is subjected to gravity and periodic lateral excitation. In-plane displacements at the boundary are constrained elastically. In the experiment, a shell-panel is used with thickness 0.24 mm, square form of length 140 mm and mean radius 5150 mm of the cylindrical surface. All edges of the rectangular boundary are supported by flexible adhesive films. Then, the boundary conditions are satisfied as the simply supported for deflection and elastic constraint for in-plane displacements. Linear natural frequencies and characteristics of restoring force of the shell-panel are measured. By shaking the shell-panel laterally with periodic acceleration, the nonlinear frequency response curves are recorded. In typical frequency ranges, chaotic time responses are detected. In the analysis, the Donnell–Mushtari–Vlasov equation, including lateral inertia force is used for a governing equation. Applying the Bobnov–Galerkin procedure, the equation is reduced to a set of nonlinear ordinary differential equations. Since the chaotic vibrations of the shell-panel inherently include higher vibration modes, multiple modes are taken into account in the analysis. Nonlinear periodic responses are calculated by the harmonic balance method. Time histories of the chaotic responses are integrated numerically by the Runge–Kutta–Gill method. Chaotic phenomena of the shallow cylindrical shell-panel are discussed by comparing the results of the experiment and the analysis. Chaotic time responses are inspected by the Fourier spectra, the Poincaré projections, the maximum Lyapunov exponents and the Lyapunov dimension.

## 2. Shallow cylindrical shell-panel and supporting condition

For the test specimen of the shallow cylindrical shell-panel, a phosphor-bronze sheet of thickness 0.198 mm is rolled to a cylindrical surface. Both surfaces of the shell-panel are painted with acrylic resin of white color. The white surface of the shell-panel enhances measuring accuracy of the deflection as a reflection target of a laser displacement sensor used in the experiment. The thickness $h$ of the shell-panel including the painted layer is $h = 0.24$ mm. The material properties of the shell-panel are measured as the Young's modulus $E$ is 62.4 GPa and the mass density $\rho$ is $7.52 \times 10^3$ kg/m$^3$ including the painted layer. The Poisson's ratio $v$ is taken as 0.33. The shell is cut to square form on the cylindrical surface. Fig. 1 shows the shallow cylindrical shell-panel and a rectangular supporting frame. The boundary condition of simply supported edges around the shell-panel is constructed with following procedure. A supporting frame, made of duralumin, of the shell-panel is fabricated to square form with inner length 140 mm. Side lengths of the shell-panel are measured as $a = 139.5$ mm and $b = 139.8$ mm. All edges of the shell-panel are connected to the supporting frame by strips of flexible adhesive film with thickness 0.072 mm. One end of the adhesive strip wraps around the edge of the shell-panel, while the

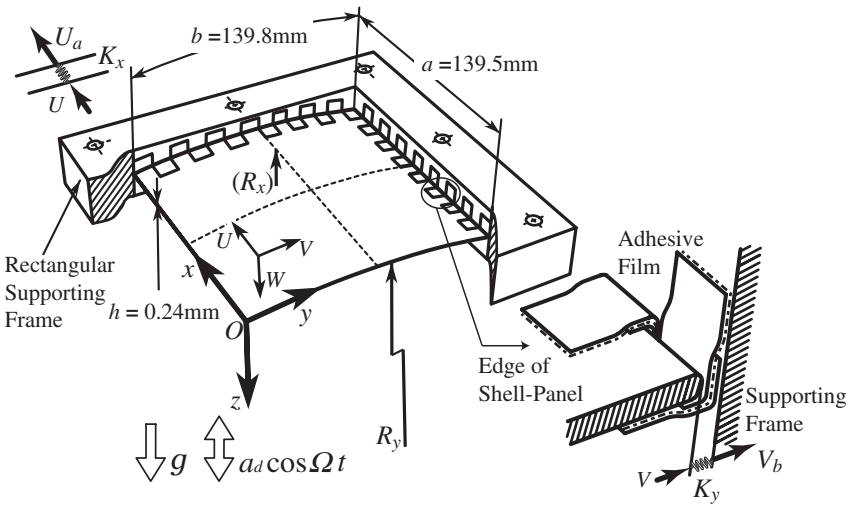


Fig. 1. Shallow cylindrical shell-panel and supporting condition.

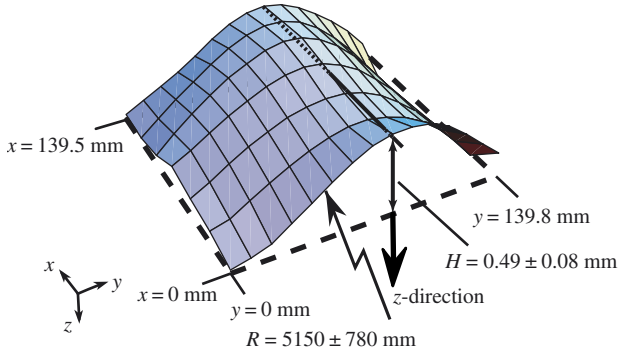


Fig. 2. The configuration of the simply supported shell-panel parallel to the gravity.

other end is glued to the inner wall of the supporting frame. The strips are glued alternately along the panel edge as shown in Fig. 1. Thus, the boundary of the shell satisfies the conditions of simply support for deflection and of elastic constraint for in-plane displacement. In the figure, the coordinate system is defined by the $x$-axis along the straight edge, the $y$-axis along the curved edge of the shell-panel and the $z$-axis perpendicular to the shell surface. In-plane displacements $U$ and $V$ are denoted along the $x$-axis and the $y$-axis, respectively. The deflection of the shell-panel is denoted by $W$ along the $z$-axis. The shell-panel is subjected to the gravitational acceleration $g$ and periodic acceleration $a_d \cos \Omega t$ in the lateral direction of the shell surface, where $a_d$, $\Omega$ and $t$ correspond to the amplitude of excitation, the exciting angular frequency and time, respectively.

In the experiment, curved configuration of the shell surface is measured by the laser displacement sensor. To minimize the static deformation by the gravitational force on the shell-panel, the initial configuration of the shell-panel is measured by setting the straight edge of the shell parallel to the gravitational direction. The configuration of the shell surface without gravitational force is shown in Fig. 2. Using the least square procedure, the circumferential configuration along the $y$-direction is approximated to cylindrical form. Radius $R$ of the shell-panel is obtained as $R = 5150 \pm 780$ mm which is much larger than the side length $b = 139.8$ mm. Raise $H$ of the cylindrical surface from the flat plane is calculated as $H = 0.49 \pm 0.08$ mm. Moreover, the configuration along the $x$-direction is slightly curved toward the $z$-direction. Consequently, the cylindrical shell-panel has partially saddle form. It is also observed that the boundary of the shell-panel has small distortion from a perfect cylindrical surface. Peak undulation of the edges is less than 0.07 mm.

For the analysis, as shown in Fig. 1, the shallow cylindrical shell-panel is assumed to be doubly curved shell-panel with radii of curvature $R_x$ and $R_y$ along the $x$-direction and the $y$-direction, respectively. The curvature $1/R_y$ is much larger than the curvature $-1/R_x$. The shell-panel is assumed to be simply supported for deflection along all edges of the rectangular boundary. For the in-plane displacement at the boundary, the edges of opposite side are assumed to be connected to in-plane springs with same stiffness. The in-plane springs are distributed perpendicular to the edges. At the curved edges $x = 0$ and $a$, the spring stiffness per unit length is denoted by $K_x$. At the straight edges $y = 0$ and $b$, in-plane springs with the stiffness $K_y$ are connected.

## 3. Procedure of experiments

Static deflection of the shell-panel appears initially under the gravity perpendicular to the shallow shell surface. The shell-panel and the supporting frame are excited laterally by the cyclic acceleration. Dynamic responses of the shell-panel relative to the supporting frame are measured. The chaotic responses are inspected precisely with the following procedure.

### 3.1. Measurement of linear natural frequencies and restoring force

As fundamental properties of the shell-panel, linear natural frequencies and characteristics of restoring force are measured.

Applying periodic acoustical pressure on the shell-panel, resonant response of small amplitude of vibration is detected by a laser displacement sensor. Natural frequencies of the shell-panel are inspected with a spectrum analyzer. Natural modes of vibration are also confirmed by scanning the sensor over the shell surface. Characteristics of restoring force of the shell-panel are examined. To obtain a relation between static deflection and static concentrated force, the laser displacement sensor and a load cell are used. The load cell consists of a dual-cantilevered beam with a tip needle-end and a strain gauge glued on the beam. Pressing the load cell to the shell-panel through the tip needle, the concentrated force is loaded on the shell. Then, the shell-panel deflects to an equilibrium position of elastic force between the shell-panel and the load cell. Consequently, the characteristics of the restoring force of the shell-panel can be identified.

### 3.2. Procedure of vibration test on chaotic responses

A schematic diagram of a vibration test apparatus is shown in Fig. 3. Whole instruments of the vibration test are numbered from 1 to 16. The cylindrical shell-panel is shaken periodically with an electromagnetic exciter through the supporting frame. The frame is fixed on a vibration head of the exciter. The excitation is provided by the devices of the Brüel and Kjaer products as numbered from 1 to 5. The exciter controller 1 (B&K 1050) generates a sinusoidal periodic signal, where the frequency of the periodic signal can be swept with the resolution of 1 mHz. The periodic signal is amplified with the power amplifier 2 (B&K 2708). The vibration exciter 3 (B&K 4802) drives the supporting frame with periodic acceleration through the exciter head 4 (B&K 4818). The accelerometer pickup 5 (B&K 4371) fixed on the frame detects the acceleration acting on the shell-panel. The signal of the acceleration is fed back to the controller 1. Then, the peak amplitude of acceleration can be kept to a prescribed constant level during a sweep of the exciting frequency. Dynamical responses of the shell-panel are measured with the instruments of the laser displacement sensor from 6 to 8 (Keyence LC2400). Relative displacement of the shell to the supporting frame is detected with the laser displacement sensors 6 and 7. The sensor 6 detects the periodic displacement of the frame. The sensor 7 measures the sum of the response of the shell-panel and the periodic displacement of the frame. The controller 8 subtracts the two signals. With this subtraction, the pure dynamic response $w(\tau)$ of the shell-panel can be detected, where $w$ and $\tau$ indicate the non-dimensional deflection and time, respectively, which will be defined in Section 4. Moreover, common-mode signals due to external disturbances can be eliminated. The laser sensor 7 is set on the sliding table 9 and the sensor moves on the surface of the shell-panel. Thus, static deflection can be measured and modal pattern of periodic response can be inspected.

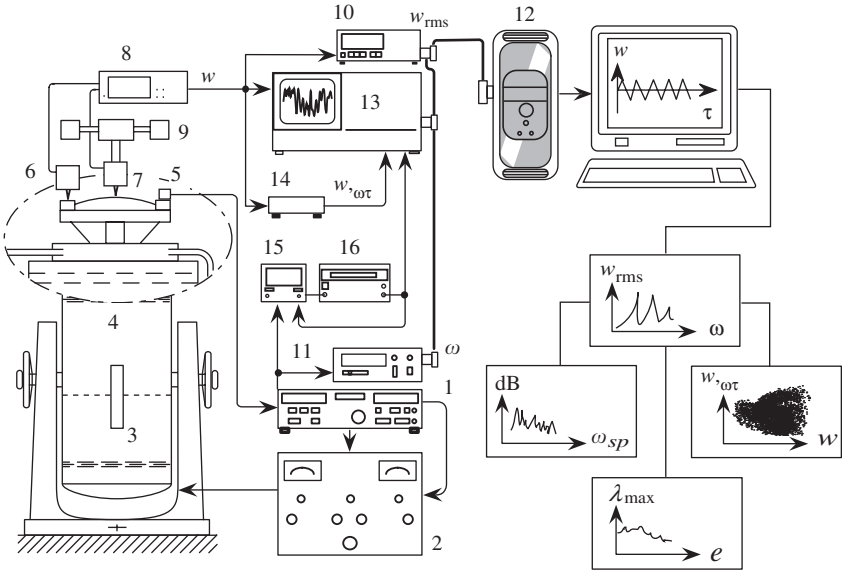


Fig. 3. Vibration test apparatus.

The instruments from 10 to 16 are the measuring devices of signal processing and data analysis. Nonlinear frequency responses of the shell-panel are obtained by sweeping the exciting frequency. The time responses of the shell-panel detected by the laser sensors are transformed to the amplitude in a root mean square value $w_{\mathrm{rms}}$ with the digital voltmeter 10 (Advantest TR6841). The exciting frequency applied on the shell-panel is counted with the digital frequency counter 11 (Advantest TR5822) through the signal of periodic acceleration measured with the accelerometer 5. The amplitude $w_{\mathrm{rms}}$ of the shell response and the exciting frequency are transferred to the computer 12 (Apple Macintosh) through the GP-IB bus-line (National Instruments GPIB-SCSI-A). The exciting frequency is normalized to the non-dimensional exciting frequency $\omega$ which is defined in Section 4. Then, the nonlinear frequency response curves are recorded with the relation between $w_{\mathrm{rms}}$ and $\omega$. The digital spectrum analyzer 13 (Advantest TR9405) records time responses of chaotic vibrations of the shell-panel. The chaotic time responses are transformed to the Fourier spectra. Furthermore, the chaotic time responses are transmitted to the computer 12 and the maximum Lyapunov exponents $\lambda_{\max}$ are calculated. The Poincaré projection of the response is obtained by the following step. Dynamic displacement of the responses is transformed to velocity by the differentiation amplifier 14. The set of the displacement $w$ and the velocity $w_{,\omega\tau}$ is recorded sequentially once in every period of the excitation. Synchronized with the period of exciting acceleration, a pulsating signal is generated with the phase meter 15 (B&K 2971) and the delayed pulse oscillator 16 (NF Elec. Instr.1930). The phase meter detects the maximum amplitude of the periodic acceleration, then the pulse oscillator generates the pulsating signal with a prescribed phase delay. The set of aforementioned displacement and velocity of the chaotic response is recorded by the analyzer 13 in each trigger by the pulsating signal. The Poincaré projections of the chaotic response are stored in the computer 12, and the projection is also displayed.

### 3.3. Thermal control of the shell-panel

The chaotic response of the shallow shell-panel is drastically influenced by a small change of the shell curvature. The curvature of the shell is intensely changed by the in-plane displacement. The in-plane displacement has same order with thermal elongation of the shell-panel, even if deviation of the temperature of the shell-panel is small. To obtain precise results of the chaotic responses, the in-plane thermal elongation of the shell-panel relative to the supporting frame should be kept constant during the vibration test. The temperatures both of the shell-panel and the supporting frame are kept constant.

Fig. 4 shows a schematic diagram of the thermal control system. The test shell-panel 1 and the supporting frame 2, in the enlarged figure, are mounted on the exciter head 3 through the cooling plate 4. The temperature of the cooling plate is stabilized by running water. Furthermore, the shell-panel and the frame are set in the air chamber 5 which is surrounded by air-formed sheets. To stabilize the temperature of the shell-panel, the temperature of ambient air of the shell-panel is controlled within very small fluctuation. Two sets of control instruments are introduced. First, The air conditioner 6 controls the temperature of the ambient air in the chamber coarsely. The conditioner controls the temperature slightly lower than a target temperature. The set of a thermal sensor and a controller 7 detects the temperature $\theta_r$ of the air in the vicinity of the shell-panel and compensates the temperature $\theta_r$ to the target temperature with the electric heater 8. The temperature $\theta_f$ of the supporting frame is stabilized by running water through the cooling plate 4. The running water flows through the hot water bath 9 and is kept to a constant temperature. Both temperatures $\theta_r$ and $\theta_f$ are recorded by the data-logger 10 and time variation of the temperatures are also monitored by the computer 11. Through the vibration test, the temperature $\theta_r$ of the ambient air close to the shell-panel is controlled to $20 \pm 0.5\,^{\circ}\mathrm{C}$, while the temperature $\theta_f$ of the supporting frame is stabilized almost constant.

To accomplish the stabilization of temperature sufficiently, the cooling plate works to isolates the supporting frame from large thermal flux transmitted through the electromagnetic exciter. The exciter exhausts huge hot air. The hot air is cooled down in a thermal reservoir as shown in the figure.

## 4. Procedure of analysis

The chaotic responses obtained by the experiment are compared with analytical results. The following procedure of theoretical analysis is introduced for the comparison.

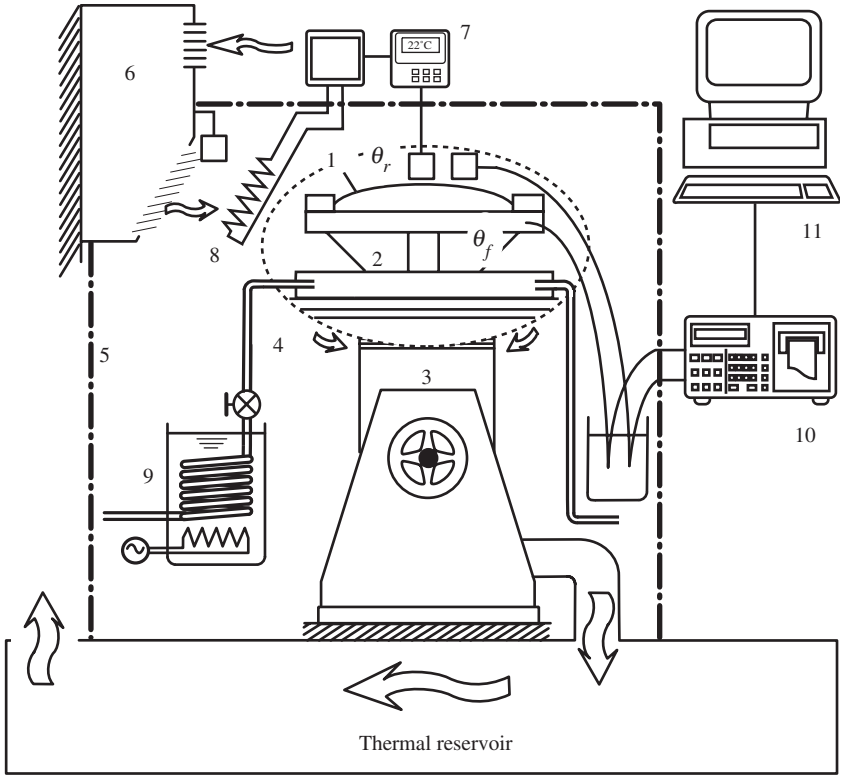


Fig. 4. Schematic diagram of thermal control system.

### 4.1. Governing equations and boundary conditions

The geometry of the shallow cylindrical shell-panel and the supporting conditions are explained in Section 2. The experiment of large amplitude vibrations of the shell-panel is restricted to lower frequency range where bending vibrations are dominant, then the effects of in-plane inertia forces can be neglected in the analysis. The Donnell–Mushtari–Vlasov type equations modified with a lateral inertia force are introduced [33,34].

Denoting the stress function by $F$ and using the deflection $W$, the non-dimensional governing equations of the shell-panel including lateral inertia force are shown as

$$\overline{\nabla}^4 f = c[\beta^2(w,^2_{\xi\eta} - w,_{\xi\xi}w,_{\eta\eta}) - \alpha_x\beta^2 w,_{\eta\eta} - \alpha_y w,_{\xi\xi}], \tag{1}$$

$$\begin{aligned} L(w,f) \equiv\ & w,_{\tau\tau} + \overline{\nabla}^4 w - \alpha_x\beta^2 f,_{\eta\eta} - \alpha_y f,_{\xi\xi} \\ & - \beta^2(f,_{\xi\xi}w,_{\eta\eta} - 2f,_{\xi\eta}w,_{\xi\eta} + f,_{\eta\eta}w,_{\xi\xi}) \\ & - (p_s + p_d\cos\omega\tau) - q_s\delta(\xi - \xi_1)\,\delta(\eta - \eta_1) = 0, \end{aligned} \tag{2}$$

where

$$\overline{\nabla}^2 \equiv \frac{\partial^2}{\partial\xi^2} + \beta^2\frac{\partial^2}{\partial\eta^2}. \tag{3}$$

Eq. (1) corresponds to the compatibility equation in terms of the stress function of the shell-panel, while Eq. (2) shows the equation of motion for the deflection coupled with the stress function. Here, using notations

$\Omega_0 = (1/a^2)\sqrt{D/\rho h}$ and $c = 12(1-\nu^2)$, the following non-dimensional quantities are introduced:

$$\begin{aligned}
[\xi, \xi_1] &= [x, x_1]/a, [\eta, \eta_1] = [y, y_1]/b,\\
\beta &= a/b, \alpha_x = a^2/R_x h, \alpha_y = a^2/R_y h,\\
w &= W/h, [u, v] = [U, V](a/h^2),\\
[n_x, n_y, n_{xy}] &= [N_x, N_y, N_{xy}](a^2/D), f = F/D,\\
[k_x, k_y] &= [K_x, K_y](ah^2/D),\\
[p_s, p_d] &= [g, a_d](\rho a^4/D), q_s = Q_s a^2\beta/Dh,\\
\tau &= \Omega_0 t, \omega = \Omega/\Omega_0.
\end{aligned} \tag{4}$$

In the foregoing, $D = Eh^3/12(1-\nu^2)$ is the bending rigidity of the shell-panel, $E$, $\nu$ and $\rho$ are the Young's modulus, the Poisson's ratio and the mass density of the shell-panel, respectively. The symbols $\xi$ and $\eta$ are the non-dimensional coordinates. The symbol $\beta$ is the aspect ratio of the length of the rectangular boundary. The symbols $\alpha_x$ and $\alpha_y$ are the non-dimensional shell curvatures in the $x$- and $y$-direction, respectively. The symbol $w$ is the non-dimensional deflection, while $u$ and $v$ are the in-plane displacements in the $\xi$- and $\eta$-direction, respectively. In Eqs. (1) and (2), subscripts following a comma denote partial differentiations. The symbols $N_x, N_y$ and $N_{xy}$ are the stress resultants acting on a cross section perpendicular to the $x$- and $y$-direction. The symbols $k_x$ and $k_y$ represent the non-dimensional coefficients of the in-plane springs attached to the curved edge ($\xi = 0$ and 1) and the straight edge ($\eta = 0$ and 1), respectively. The symbols $p_s$ and $p_d$ correspond to the non-dimensional intensity of distributed force by the gravitational acceleration $g$ and the periodic acceleration $a_d$, respectively. The symbol $q_s$ is the non-dimensional concentrated force. When the characteristics of restoring force of the shell-panel are examined, the concentrated force $Q_s$ is loaded at the point $x_1$ and $y_1$. The symbols $\omega$ and $\tau$ are the non-dimensional exciting frequency and the non-dimensional time, respectively. The non-dimensional stress resultants $n_x, n_y$ and $n_{xy}$ are related to the stress function $f$ as

$$n_x = \beta^2 f_{,\eta\eta}, n_y = f_{,\xi\xi}, n_{xy} = -\beta f_{,\xi\eta}. \tag{5}$$

The in-plane displacements $u$ and $v$ are related to $w, w_0$ and $f$ as

$$\begin{aligned}
c[u_{,\xi} - \alpha_x w + (\tfrac{1}{2})w_{,\xi}^2] &= \beta^2 f_{,\eta\eta} - \nu f_{,\xi\xi},\\
c[\beta v_{,\eta} - \alpha_y w + (\beta^2/2)w_{,\eta}^2] &= f_{,\xi\xi} - \nu\beta^2 f_{,\eta\eta},\\
c[\beta u_{,\eta} + v_{,\xi} + \beta w_{,\xi} w_{,\eta}] &= -2\beta(1+\nu) f_{,\xi\eta}.
\end{aligned} \tag{6}$$

The deflection along the all edges of the rectangular boundary is assumed to be simply supported:

$$\begin{aligned}
\xi = 0, 1:\ & w = 0, w_{,\xi\xi} = 0,\\
\eta = 0, 1:\ & w = 0, w_{,\eta\eta} = 0.
\end{aligned} \tag{7}$$

The in-plane boundary conditions are assumed as

$$\begin{aligned}
\xi = 0:\ & \int_0^1 [n_x - k_x(u - u_0)]\,\mathrm{d}\eta = 0, \quad \int_0^1 n_{xy}\,\mathrm{d}\eta = 0,\\
\xi = 1:\ & \int_0^1 [n_x + k_x(u - u_a)]\,\mathrm{d}\eta = 0, \quad \int_0^1 n_{xy}\,\mathrm{d}\eta = 0,\\
\eta = 0:\ & \beta\int_0^1 [n_y - k_y(v - v_0)]\,\mathrm{d}\xi = 0, \quad \beta\int_0^1 n_{xy}\,\mathrm{d}\xi = 0,\\
\eta = 1:\ & \beta\int_0^1 [n_y + k_y(v - v_b)]\,\mathrm{d}\xi = 0, \quad \beta\int_0^1 n_{xy}\,\mathrm{d}\xi = 0.
\end{aligned} \tag{8}$$

In the above conditions, $u_0, u_a, v_0$ and $v_b$ are the initial in-plane displacements for the outer part of the in-plane springs connected to the edges of the shell-panel. The in-plane stress resultant and the restoring force of the in-plane spring are in equilibrium with averaged form along the boundary [35]. The dynamical analysis consists of finding the solutions $w$ and $f$ which satisfy the governing equations and the boundary conditions.

### 4.2. Reduction to multiple-degree-of-freedom system

The Bobnov–Galerkin procedure is applied to reduce the governing equations to the equations of a multiple-degree-of-freedom system. The deflection $w$ of the shell-panel is assumed as

$$w(\xi,\eta,\tau)=\sum_m\sum_n \hat{b}_{mn}(\tau)\hat{\zeta}_{mn}(\xi,\eta), \quad (m,n=1,2,3,\ldots),$$
$$\hat{\zeta}_{mn}(\xi,\eta)=\sin m\pi\xi \sin n\pi\eta, \tag{9}$$

where $\hat{b}_{mn}$ is an unknown time function, while $\hat{\zeta}_{mn}$ is the coordinate function. The indices $m$ and $n$ imply the half-wavenumbers of the coordinate function along the $x$- and $y$-axis, respectively. The solution of the compatibility equation (1) can be expressed as

$$\begin{aligned} f=&(\tfrac{1}{2})p_y\xi^2+(\tfrac{1}{2})p_x\eta^2+p_{xy}\xi\eta\\ &+\sum_m\sum_n d^{(0)}_{mn}\hat{b}_{mn}\sin\overline{m}\xi\sin\overline{n}\eta\\ &+\sum_k\sum_l\sum_m\sum_n \hat{b}_{kl}\hat{b}_{mn}\{\theta^{(1)}_{klmn}\cos(\overline{k}-\overline{m})\,\xi\cos(\overline{l}-\overline{n})\eta\\ &+\theta^{(2)}_{klmn}\cos(\overline{k}-\overline{m})\,\xi\cos(\overline{l}+\overline{n})\eta+\theta^{(3)}_{klmn}\cos(\overline{k}+\overline{m})\,\xi\cos(\overline{l}-\overline{n})\eta\\ &+\theta^{(4)}_{klmn}\cos(\overline{k}+\overline{m})\,\xi\cos(\overline{l}+\overline{n})\eta\} \quad (k,l,m,n=1,2,3,\ldots), \end{aligned} \tag{10}$$

where the notation $\overline{m}=m\pi$ is introduced and the symbols $d^{(0)}_{mn}$ and $\theta^{(i)}_{klmn}$ $(i=1,2,3,4)$ are listed in Appendix A.

In the foregoing equation, $p_x, p_y$ and $p_{xy}$ are arbitrary time functions. Substituting Eqs. (9) and (10) into Eq. (6), the in-plane displacements $u$ and $v$ are derived. The time functions $p_x, p_y$ and $p_{xy}$ are reduced with the in-plane boundary condition of Eq. (8) as

$$\begin{aligned} p_y&=\sum_m\sum_n\{d^{(1)}_{mn}\hat{b}_{mn}+e^{(1)}_{mn}\hat{b}^2_{mn}\}+g_1,\\ p_x&=\sum_m\sum_n\{d^{(2)}_{mn}\hat{b}_{mn}+e^{(2)}_{mn}\hat{b}^2_{mn}\}+g_2,\\ p_{xy}&=0, \end{aligned} \tag{11}$$

where $d^{(i)}_{mn}, e^{(i)}_{mn}$ and $g_i$, $(i=1,2)$ are functions related to the shell geometry, the in-plane spring stiffness and the initial in-plane displacements, which are listed in Appendix B. In the foregoing procedure, $w$ and $f$ are expressed with the unknown time function $\hat{b}_{mn}(\tau)$. The Galerkin procedure is applied to the equation of motion (2), the following condition is derived for the coordinate function $\hat{\zeta}_{rs}$ as:

$$\int_0^1\int_0^1 L(w,f)\hat{\zeta}_{rs}(\xi,\eta)\,\mathrm{d}\xi\,\mathrm{d}\eta=0 \quad (r,s=1,2,3,\ldots). \tag{12}$$

Substituting both Eqs. (9) and (10) into Eq. (12) and performing the integration, the set of nonlinear ordinary differential equations, in terms of $\hat{b}_{mn}(\tau)$, is reduced

$$\begin{aligned} &\sum_m\sum_n \hat{B}_{rsmn}\hat{b}_{mn,\tau\tau}+\sum_m\sum_n \hat{C}_{rsmn}\hat{b}_{mn}+\sum_k\sum_l\sum_m\sum_n \hat{D}_{rsklmn}\hat{b}_{kl}\hat{b}_{mn}\\ &+\sum_i\sum_j\sum_k\sum_l\sum_m\sum_n \hat{E}_{rsijklmn}\hat{b}_{ij}\hat{b}_{kl}\hat{b}_{mn}-\hat{F}_{rs}-(p_s+p_d\cos\omega\tau)\hat{G}_{rs}=0,\\ &(r,s,i,j,k,l,m,n=1,2,3,\ldots). \end{aligned} \tag{13}$$

In the foregoing, $\hat{B}_{rsmn}$ is the coefficient of inertia term, while the coefficients $\hat{C}_{rsmn}$, $\hat{D}_{rsklmn}$ and $\hat{E}_{rsijklmn}$ correspond to the restoring forces of linear, quadratic and cubic terms, respectively. The $\hat{F}_{rs}$ is the constant coefficient and $\hat{G}_{rs}$ is related to the term of periodic excitation. These coefficients include the parameters of the shell geometry and the in-plane spring, which are listed in Appendix C. The suffices $r$ and $s$ of the coefficients in Eq. (13) imply the half-wavenumbers of the configuration of deflection in the $\xi$-direction and $\eta$-direction, respectively. A combination of the suffices $r$ and $s$ represents the modal pattern of deflection, which can be referred as a new index $i$. The unknown time function $\hat{b}_{mn}(\tau)$ is corresponded to a new variable $\check{b}_j(\tau)$, and the corresponding coefficients are also renumbered as follows:

$$\begin{aligned}&\check{b}_j \equiv \hat{b}_{mn}, \check{\zeta}_j \equiv \hat{\zeta}_{mn}, \check{B}_{ij} \equiv \hat{B}_{rsmn}, \check{C}_{ij} \equiv \hat{C}_{rsmn},\\ &\check{D}_{ijk} \equiv \hat{D}_{rsklmn}, \check{E}_{ijkl} \equiv \hat{E}_{rsijklmn}, \check{F}_i \equiv \hat{F}_{rs}, \check{G}_i \equiv \hat{G}_{rs}.\end{aligned} \tag{14}$$

These variables and coefficients are counted in the order of a set of the half-wavenumbers of the shell-configuration. For example, $\hat{b}_{11}, \hat{b}_{12}$ and $\hat{b}_{21}$ are referred as $\check{b}_1, \check{b}_2$ and $\check{b}_3$, respectively. Eq. (13) can be rearranged as follows:

$$\begin{aligned}&\sum_j \check{B}_{ij}\check{b}_{j,\tau\tau} + \sum_j \check{C}_{ij}\check{b}_j + \sum_j \sum_k \check{D}_{ijk}\check{b}_j\check{b}_k + \sum_j \sum_k \sum_l \check{E}_{ijkl}\check{b}_j\check{b}_k\check{b}_l\\ &\quad - \check{F}_i - (p_s + p_d \cos\omega\tau)\check{G}_i = 0 \quad (i,j,k,l = 1,2,3,\ldots).\end{aligned} \tag{15}$$

Corresponding to Eq. (9), the deflection is expressed as

$$w(\xi,\eta,\tau) = \sum_j \check{b}_j(\tau)\check{\zeta}_j(\xi,\eta) \quad (j = 1,2,3,\ldots). \tag{16}$$

The dynamic responses of the shallow shell-panel are strongly influenced by static deformation. The static deformation is due to the static forces $p_s$ and the in-plane constraint at the boundary. Hence, the static deformation and the dynamic responses are solved by the following sequential procedure. First, the deflection $w(\xi,\eta,\tau)$ of the shell-panel is divided into the static deflection $\overline{w}(\xi,\eta)$ and to the dynamic displacement $\tilde{w}(\xi,\eta,\tau)$ as

$$w(\xi,\eta,\tau) = \overline{w}(\xi,\eta) + \tilde{w}(\xi,\eta,\tau). \tag{17}$$

The static deflection and the dynamic displacement are assumed as follows:

$$\begin{aligned}&\overline{w}(\xi,\eta) = \sum_j \overline{b}_j\check{\zeta}_j(\xi,\eta),\\ &\tilde{w}(\xi,\eta,\tau) = \sum_j \tilde{b}_j(\tau)\check{\zeta}_j(\xi,\eta) \quad (j = 1,2,3,\ldots),\end{aligned} \tag{18}$$

where $\overline{b}_j$ is an unknown constant and $\tilde{b}_j(\tau)$ represents an unknown time function of the dynamic displacement measured from the static equilibrium position. From Eq. (16) to Eq. (18), the variable $\check{b}_j(\tau)$ is expressed as $\check{b}_j(\tau) = \overline{b}_j + \tilde{b}_j(\tau)$. Then, substituting this relation to Eq. (15), the following two sets of coupled equations are obtained:

$$\sum_j \check{C}_{ij}\overline{b}_j + \sum_j \sum_k \check{D}_{ijk}\overline{b}_j\overline{b}_k + \sum_j \sum_k \sum_l \check{E}_{ijkl}\overline{b}_j\overline{b}_k\overline{b}_l - \check{F}_i - p_s\check{G}_i = 0 \quad (i,j,k,l = 1,2,3,\ldots), \tag{19}$$

$$\sum_j \check{B}_{ij}\tilde{b}_{j,\tau\tau} + \sum_j \tilde{C}_{ij}\tilde{b}_j + \sum_j \sum_k \tilde{D}_{ijk}\tilde{b}_j\tilde{b}_k + \sum_j \sum_k \sum_l \check{E}_{ijkl}\tilde{b}_j\tilde{b}_k\tilde{b}_l - p_d\cos\omega\tau\check{G}_i = 0 \quad (i,j,k,l = 1,2,3,\ldots), \tag{20}$$

where

$$\begin{aligned}&\tilde{C}_{ij} = \check{C}_{ij} + \sum_k (\check{D}_{ijk} + \check{D}_{ikj})\overline{b}_k + \sum_k \sum_l (\check{E}_{ijkl} + \check{E}_{iljk} + \check{E}_{iklj})\overline{b}_k\overline{b}_l,\\ &\tilde{D}_{ijk} = \check{D}_{ijk} + \sum_l (\check{E}_{ijkl} + \check{E}_{iljk} + \check{E}_{iklj})\overline{b}_l \quad (i,j,k,l = 1,2,3,\ldots).\end{aligned} \tag{21}$$

Eq. (19) is the set of cubic equations in terms of $\overline{b}_j$ under the in-plane constraint and the static force $p_s$. The static deflection $\overline{w}(\xi,\eta)$ can be obtained by the solution $\overline{b}_j$ using Eq. (19). Eq. (20) is the equation of motion in terms of the new coordinate $\tilde{b}_j$ which is measured from the static equilibrium position. In the equation, the restoring forces of a linear spring and of a quadratic nonlinear spring are influenced by the static deflection.

Furthermore, omitting the nonlinear terms as well as the terms of external periodic force, the linear equation is obtained for free vibration. The linear natural frequencies $\omega_i$ and corresponding eigenvectors $\phi_{ip}, (p = 1, 2, 3, \ldots)$ are obtained. The linear natural mode of vibration $\tilde{\zeta}_i$, corresponding to $\omega_i$, is expressed as follows:

$$\tilde{\zeta}_i(\xi,\eta) = \frac{1}{n_i}\sum_q \psi_{qi}\breve{\zeta}_q(\xi,\eta),$$

$$\psi_{qi} = \phi_{iq}\left[\sum_k\sum_l \phi_{ik}\breve{B}_{kl}\phi_{il}\right]^{-\frac{1}{2}} \quad (i,k,l,q = 1,2,3,\ldots), \tag{22}$$

where $n_i$ is an arbitrary constant chosen to normalize the maximum amplitude of natural mode to unity. For the analyses of the dynamic responses, Eq. (20) is transformed to a new set of nonlinear differential equations. Using the normal coordinates $b_i$ corresponding to $\tilde{\zeta}_i$, the deflection $\tilde{w}$ measured from the static equilibrium point can be expressed as

$$\tilde{w}(\xi,\eta,\tau) = \sum_i b_i(\tau)\tilde{\zeta}_i(\xi,\eta) \quad (i = 1,2,3,\ldots). \tag{23}$$

Transforming the coordinate $\tilde{b}_j$ to the normal coordinate $b_i$, one can obtain a set of nonlinear differential equations in the standard form:

$$M(b_i) \equiv b_{i,\tau\tau} + 2\varepsilon_i\omega_i b_{i,\tau} + \omega_i^2 b_i + \sum_j\sum_k D_{ijk}b_j b_k + \sum_j\sum_k\sum_l E_{ijkl}b_j b_k b_l - p_d G_i\cos\omega\tau = 0, \quad (i,j,k,l = 1,2,3,\ldots), \tag{24}$$

where

$$D_{ijk} = \frac{n_i}{n_j n_k}\sum_p\sum_q\sum_r \tilde{D}_{pqr}\psi_{pi}\psi_{qj}\psi_{rk},$$

$$E_{ijkl} = \frac{n_i}{n_j n_k n_l}\sum_p\sum_q\sum_r\sum_s \breve{E}_{pqrs}\psi_{pi}\psi_{qj}\psi_{rk}\psi_{sl},$$

$$G_i = n_i\sum_p \psi_{pi}\breve{G}_p \quad (p,q,r,s = 1,2,3,\ldots). \tag{25}$$

The foregoing Eq. (24) has couplings only in the quadratic and cubic nonlinear terms. A linear damping term is introduced, where $\varepsilon_i$ represents a damping ratio corresponding to $i$th linear mode of vibration.

In the numerical calculations of the static deformation in Eq. (19) as well as of the linear natural frequencies in Eq. (20) by omitting the nonlinear and forcing terms, finite terms of unknown variables $\overline{b}_j$ and $\tilde{b}_j$ are required up to the maximum term $M$. The maximum term $M$ of the variable corresponds to the set of the maximum half-wavenumbers of $\hat{b}_{mn}$ in Eq. (9). After the transformation to the standard form of Eq. (24), the nonlinear dynamical responses can be calculated with the reduced number of modes $I_c$ less than the number $M$, without loosing the numerical accuracy in relatively lower frequency range.

### 4.3. Determination of periodic responses

Predominant chaotic responses are bifurcated from sub-harmonic resonance responses of $\frac{1}{2}$ and $\frac{1}{3}$ orders for the beam and the arch [23,24]. Therefore, it is of importance to evaluate the periodic responses of the shell-panel. The periodic responses are calculated by the harmonic balance method [36]. The periodic solution $b_i$ is

assumed as

$$b_i = C_{i1\mu 0} + \sum_p [C_{i1\mu p} \cos \mu p\omega\tau + C_{i2\mu p} \sin \mu p\omega\tau], \quad (i = 1, 2, 3, \ldots, I_c,\ p = 1, 2, 3, \ldots), \tag{26}$$

where $C_{i1\mu 0}$, $C_{i1\mu p}$ and $C_{i2\mu p}$ are unknown constants. To obtain the solutions of principal resonance and super-harmonic resonance, $\mu$ is chosen as unity, while to get sub-harmonic resonance responses of $\frac{1}{2}$ or $\frac{1}{3}$ orders, $\mu$ is taken as $\frac{1}{2}$ or $\frac{1}{3}$, respectively. Substituting Eq. (26) into Eq. (24) and using the harmonic balance method, a set of coupled nonlinear equations is reduced for the unknown coefficients $C_{i1\mu 0}$, $C_{i1\mu p}$ and $C_{i2\mu p}$. The solutions of the coupled equation are determined with the Newton–Raphson method. Amplitude of the resonance is expressed as a root mean square value $\tilde{w}_{\mathrm{rms}}$:

$$\tilde{w}_{\mathrm{rms}} = \left\{ \frac{1}{2} \sum_p \left[ \left( \sum_i C_{i1\mu p} \tilde{\zeta}_i \right)^2 + \left( \sum_i C_{i2\mu p} \tilde{\zeta}_i \right)^2 \right] + \left( \sum_i C_{i1\mu 0} \tilde{\zeta}_i \right)^2 \right\}^{\frac{1}{2}} \quad (p = 1, 2, 3, \ldots; i = 1, 2, 3, \ldots). \tag{27}$$

### 4.4. Time histories of chaotic responses

Chaotic vibrations show random-like non-periodic responses. Therefore, to determine chaotic responses, it is required to integrate numerically the nonlinear ordinary differential equation (24). Denoting the unknown time function of the displacement $b_i$ as $b_i^{(1)}$, Eq. (24) is transformed into a set of state equations of first order as

$$\begin{aligned} b_{i,\tau}^{(1)} &= b_i^{(2)}, \\ b_{i,\tau}^{(2)} &= -2\varepsilon_i \omega_i b_i^{(2)} - \omega_i^2 b_i^{(1)} - \sum_j \sum_k D_{ijk} b_j^{(1)} b_k^{(1)} \\ &\quad - \sum_j \sum_k \sum_l E_{ijkl} b_j^{(1)} b_k^{(1)} b_l^{(1)} + p_d G_i \cos \omega\tau \quad (i, j, k, l = 1, 2, 3, \ldots, I_c), \end{aligned} \tag{28}$$

where $b_i^{(2)}$ stands for the velocity of $b_i^{(1)}$. Eq. (28) is integrated numerically with the Runge–Kutta–Gill method. Chaotic time responses are obtained in restricted frequency domains related to the exciting amplitude.

## 5. Evaluation of chaotic responses

Since chaotic vibrations show random-like non-periodic responses, many types of inspection are required to confirm the chaotic responses of the shell-panel. A Fourier spectrum of a non-periodic time response shows a broadband spectrum. However, predominant components of the chaotic response are related to the periodic resonance response from which the chaotic response is bifurcated. The Poincaré projections of the chaotic responses show a scattered figure on the phase plane. Furthermore, the projection focuses on a fractal pattern corresponding to types of chaos.

The Lyapunov exponent is one of the best criteria to confirm the chaotic response. It is defined as the exponential growth rate of the distance between two neighboring trajectories, namely, fiducial and nearby trajectories, in the phase space of a dynamical system. If the Lyapunov exponents have one or more positive values, the response can be confirmed as chaos. The Lyapunov exponents are calculated with the procedure proposed by Wolf et al. [37]. The Lyapunov dimension $d_L$, which shows a fractal feature of chaos, can also be calculated by the Lyapunov exponents [38]. Furthermore, number of predominant vibration modes, which contributes to the chaos, can be estimated by the convergence of the Lyapunov dimension or the maximum Lyapunov exponent when the assumed dimension of the phase space is increased [39].

In the analysis, the phase space is composed of the $2I_c$ state variables $b_i^{(p)}, (p = 1, 2; i = 1, 2, 3, \ldots, I_c)$ of the governing equation of motion in the standard form. The fiducial trajectory is calculated by the numerical integration of the equation of motion (Eq. (28)). A set of $2I_c$ normalized orthogonal vectors is selected as the set of initial variational vectors of the nearby trajectories from the fiducial trajectory. The time progress of the

variational vectors is calculated by numerically integrating the linearized variational equation. Then the exponential growth rates of the Euclidean norms of the variational vectors are evaluated in each infinitesimal time interval. The exponential growth rates are averaged in the long time interval, then the $2I_c$ Lyapunov exponents $\lambda_r, (r = 1, 2, 3, \ldots, I_c)$ can be calculated.

In the experiment, $e$-dimensional pseudo-phase space is composed with time-delay coordinates from an time response, where $e$ is the embedding dimension [40]. A component of the pseudo-phase space is a sequential time history chosen partially from the time response which has a fixed time delay from the former component. A trajectory in the pseudo-phase space is constructed from the single time response of the shell-panel from an arbitrary start time. Two trajectories, which initially have sufficiently small distance, are selected as the fiducial trajectory and the nearby trajectory. The exponential growth rate of the distance between the two trajectories is calculated in each infinitesimal time interval. The exponential growth rate is averaged in the long time interval, then the maximum Lyapunov exponent $\lambda_{\max}$ can be estimated.

## 6. Results and discussion

### 6.1. Fundamental properties of the shell-panel

Chaotic responses of the shallow cylindrical shell-panel are influenced drastically by small deviations of the shell curvature, the boundary condition for deflection and the in-plane constraint at the boundary. It is essential that the geometrical parameters of the shell-panel are precisely measured in the experiment. However, some parameters cannot be measured directly. Then, the geometrical parameters of the shell-panel are indirectly identified by comparing the experimental results and the analytical results. The following results are used for the identification; the configuration of the shell surface, the linear natural frequencies and the characteristics of restoring force.

The non-dimensional curvature of the shell-panel without the gravitational force is calculated as $\alpha_y = 16.2 \pm 2.6$ by the measurement in Section 2. Fig. 5 shows the deformed configuration of the shell-panel under the gravity force $p_s = 359$. The shell-panel has large deflection by the snap-through buckling by the gravity force. The deflection shows nearly symmetric to the center of the shell-panel. Then, assuming the shell-panel has the symmetric configuration to the center, the parameters are identified with many trials of computation. Following quantities of the geometrical parameters have been identified for the shallow cylindrical shell-panel including the slight saddle form

$$\alpha_y = 15, \alpha_x = -1, k_x = 0.01, k_y = 0.001, u_0 = u_a = 0, v_0 = v_b = 0, \tag{29}$$

where $u_0, u_a, v_0$ and $v_b$ are the initial in-plane displacements of the outer part of the in-plane springs. To determine the linear natural frequencies and the static deflection of the shell-panel, 25 terms are assumed for the modal expansion in Eq. (9), i.e., $M = 25$, where integers $m$ and $n$ cover from one to five.

Table 1 shows the linear natural frequencies corresponding to vibration in small amplitude. In the table, $f_{mn}$ indicates the actual frequency measured by Hz, while $\omega_{mn}$ stands for the non-dimensional frequency.

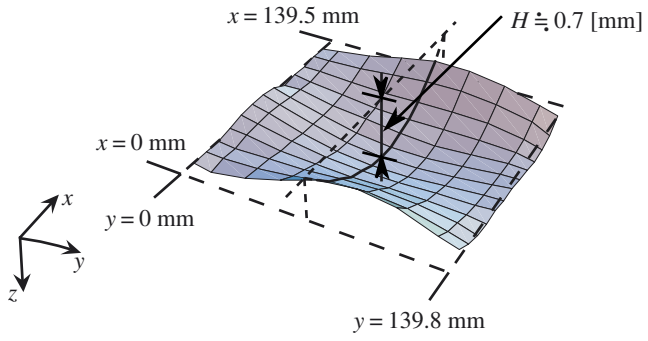


Fig. 5. The deformed configuration of the shell-panel under the gravity.

Table 1
Natural frequencies and vibration modes of the cylindrical shell

| Mode $(m,n)$ | Modal pattern $\eta$ $\xi$ | Experimental | | Analytical |
|---|---|---|---|---|
| | | $f_{mn}$ (Hz) | $\omega_{mn}$ | $\tilde{\omega}_{mn}$ |
| (1,1) | | 46.3 | 27.3 | 27.3 |
| (2,1) | | 88.8 | 52.3 | 51.1 |
| (1,2) | | 112 | 66.2 | 64.7 |
| (2,2) | | 151 | 89.2 | 75.6 |

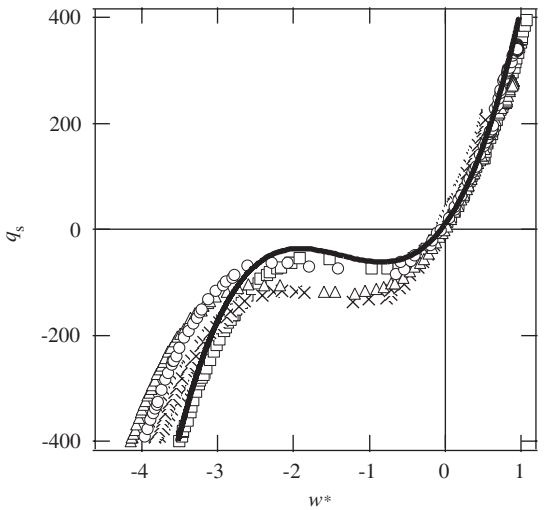


Fig. 6. Static deflection of the shell by a concentrated load: experimental results, ◯ measured at $\xi = 0.6, \eta = 0.4$, △ measured at $\xi = 0.6, \eta = 0.6$, □ measured at $\xi = 0.4, \eta = 0.6$ and × measured at $\xi = 0.4, \eta = 0.4$. Analytical result, — measured at $\xi = 0.6, \eta = 0.6$.

The integers $m$ and $n$ denote half-wavenumbers of vibration-mode along $\xi$-axis and $\eta$-axis, respectively. Modal patterns related to the natural modes of vibration are shown with the notation $(m,n)$. Linear natural frequencies $\tilde{\omega}_{mn}$ by the analysis are also listed in the table. The natural frequency $\omega_{12}$ corresponding to the third mode (1,2) is higher than that of the second mode (2,1) by the effects of the shell curvature and the static deflection. The linear natural frequencies $\omega_{mn}$ of the modes (1,1), (2,1) and (1,2) obtained by the experiment are well adapted to the analytical results within the discrepancy of 1.5 percent on average. The discrepancy between the experimental results and the analytical results of the natural frequency of the mode (2,2) is larger than those of the other lower vibration modes. The discrepancy seems to be caused by the initial deformation of the shell-panel with higher asymmetric configuration to the center of the shell-panel. Fig. 6 shows the characteristics of restoring force. The static deflections $w^*(\xi,\eta)$ of the shell-panel is shown by the concentrated force $q_s$ acting on the center of the shell-panel. The deflections are measured from the static equilibrium positions on the shell surface under the gravity force at four points on the shell-panel. The deflections $w^*$ at the symmetric points ($\xi = 0.6$, $\eta = 0.4$), (0.6, 0.6), (0.4, 0.6) and (0.4, 0.4) to the center are marked by circle, triangle, square and cross, respectively.

Analytical result of the restoring force at the point $\xi = 0.6$ and $\eta = 0.6$ is denoted by the solid line. When the deflection of the shell-panel is increased to the negative $z$-direction from the equilibrium position by the concentrated force opposite to the direction of gravity, the gradient of curve of the restoring force decreases. Then the characteristics of a softening spring appear. Furthermore, the gradient of curve changes from zero to negative. The negative slope is involved from $w = -0.8$ to $-1.9$ in the curve. As the deflection increases larger

to negative $z$-direction from $w = -1.9$, the restoring force of the shell-panel exhibits the type of a hardening spring. Consequently, the shell-panel with large deflection has the spring characteristics of a softening-and-hardening spring involving partially negative gradient.

The characteristics of restoring force in the experiment agree fairly well with the analytical results within relatively small deflection. Furthermore, regions of the negative slope in the curves are also in good agreement. However, in the experiment, the deflections at the four points in larger deformation have discrepancy, even though the concentrated force is loaded on the center of the shell-panel. The discrepancy is due to the imperfect configuration of the shell-panel. Asymmetric deformation can be induced easily by the concentrated force. In the analysis, the shell-panel is assumed to be a symmetric configuration to the center. In both experiment and analysis, the existence of the negative slope in the restoring force contributes to the generation of chaotic response in the shell-panel.

### 6.2. Frequency response curves of the shell-panel

To examine the occurrence of chaotic responses bifurcated from resonance responses, nonlinear frequency response curves of the shell-panel are inspected under the gravitational force $p_s = 359$ and the periodic exciting force $p_d \cos \omega\tau$. The amplitude of excitation $p_d$ is kept constant $p_d = 490$. Nonlinear frequency-response curves by the experiment and the analysis are shown in Figs. 7(a) and (b), respectively. In the figure, the abscissa indicates the exciting frequency $\omega$ which covers the range from $\omega = 20$ to 90. Natural frequencies of the shell-panel are also indicated by the solid circles to the abscissa. In addition, actual exciting frequency $f_{\mathrm{ex}} = \Omega/2\pi$ measured with Hz is indicated. The ordinate shows the non-dimensional amplitude $\tilde{w}_{\mathrm{rms}}$ of the responses with a root mean square value of the deflection $\tilde{w}$ at the position $\xi = 0.6$ and $\eta = 0.6$. The frequency of the excitation is swept very slowly to avoid transient effects on the chaotic response of the shell-panel in the

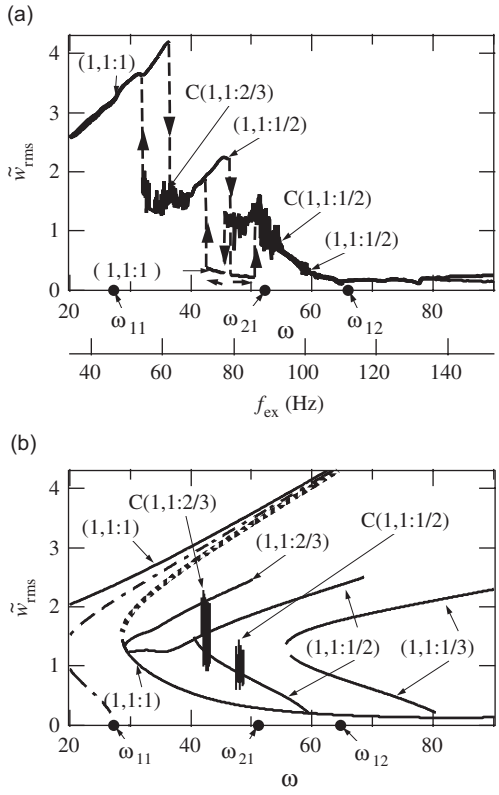


Fig. 7. Frequency response curve of the cylindrical shell-panel ($p_d = 490$, measured at $\xi = 0.6, \eta = 0.6$): (a) experimental results, (b) analytical results.

experiment. The amplitude $\tilde{w}_{\mathrm{rms}}$ is measured with relatively long time interval. In Fig. 7(a) of the experiment, the solid line indicates the frequency response curve, while the dotted line show the frequencies where jump phenomena occur. In typical frequency ranges, non-periodic response is generated with amplitude modulation of $\tilde{w}_{\mathrm{rms}}$. In Fig. 7(b) of the analysis, the thick solid lines indicate the frequency response curves of the stable periodic responses obtained by the harmonic balance method. For the computation of nonlinear dynamical responses, first six modes are considered, i.e., $I_c = 6$, within relatively lower exciting frequency range. Linear damping ratios for individual modes are assumed as $\varepsilon_i = 0.008, (i = 1, 2, \ldots, 6)$. The dotted line indicates the unstable periodic response which is evaluated with the vertical tangency of the frequency response curve. The dashed-and-dotted line indicated the backbone curve of nonlinear free vibration corresponding to the lowest mode of vibration. The non-stationary amplitudes of the chaotic responses are indicated with thin solid lines. The chaotic responses are calculated with the numerical integration. The amplitudes of the chaotic response are shown in the figure averaged within every short time intervals. Comparing the frequency response curves of the experiment with the response curves by the analysis, the type of the periodic resonance is determined by the notation $(m, n : j)$. Former indices $m$ and $n$ indicate the mode of vibration generated in the resonance, while index $j$ stands for the order of the periodic resonance. For example, (1,1:1) indicates the response of the principal resonance corresponding to the lowest mode of vibration (1, 1), while (1,1:1/2) means the sub-harmonic resonance of $\frac{1}{2}$ order.

In Fig. 7(a) of the experiment, when the exciting frequency is decreased from $\omega = 90$ in the higher frequency range, the non-resonant response prevails. Close to the frequency $\omega = 60$, the steady-state periodic response of the sub-harmonic resonance (1,1:1/2) is generated. When the frequency is $\omega = 55.3$, the non-periodic response is generated. The response is bifurcated from the sub-harmonic resonance (1,1:1/2) and is confirmed as the chaotic vibration with the evaluation methodology of chaotic responses in Section 5. The chaotic response is denoted by the notation C$(m, n : j)$, where $(m, n : j)$ represents the dominant mode of vibration and the predominant type of resonance excited in the chaotic vibration. The chaotic response C(1,1:1/2) covers the frequency from $\omega = 55.3$ to 45.5. Then, the response jumps to the non-resonant response with the lowest mode of vibration at $\omega = 45.5$. Furthermore, the periodic response of the sub-harmonic resonance (1,1:1/2) is generated again at the frequency $\omega = 42.5$ by the jump phenomenon. The frequency response curve of the sub-harmonic resonance of the lowest mode of vibration shows the type of a softening-and-hardening spring. Moreover, a new type of chaotic response C(1,1:2/3) is bifurcated from the sub-harmonic resonance response (1,1:1/2) at the frequency $\omega = 39.6$. This chaotic response corresponds to the ultra-sub-harmonic resonance response (1,1:2/3) and continues within the frequency from $\omega = 39.6$ to 31.8. Finally, the chaotic response is transited to the large amplitude periodic vibration of the principal resonance (1,1:1) through the jump phenomenon.

When the exciting frequency is increased from the lower frequency range, the large amplitude response of the principal resonance (1,1:1) jumps to the aforementioned chaotic response C(1,1:2/3) at the frequency $\omega = 36.5$. As the exciting frequency approaches $\omega = 46.5$, the sub-harmonic response (1,1:1/2) jumps directly to the non-resonant response. Furthermore, the non-resonant response jumps again to the chaotic response C(1,1:1/2) at $\omega = 50.6$.

In Fig. 7(b) of the analysis, the chaotic responses of type C(1,1:1/2) are generated within the frequency range from $\omega = 51.6$ to 47.5. The chaotic response is bifurcated from the periodic response of the sub-harmonic resonance (1,1:1/2). Furthermore, the other chaotic responses of the type C(1,1:2/3) are also generated within the range from $\omega = 44.6$ to 41.0. The non-stationary amplitudes of the chaotic response C(1,1:2/3) overlap on the response curves of the sub-harmonic resonance (1,1:1/2) and the ultra-sub-harmonic resonance (1,1:2/3). The generation of the chaotic responses is summarized as:

(1) Because of the characteristics of restoring force of a softening-and-hardening spring of the shell-panel, the dominant chaotic responses are bifurcated from the response of sub-harmonic resonances of order $\frac{1}{2}$ and from the response of ultra-sub-harmonic resonance of order $\frac{2}{3}$.
(2) In the experiment, when the exciting frequency is decreased, the chaotic responses are easily bifurcated from the sub-harmonic resonance response or ultra-sub-harmonic resonance response. While the frequency is increased, the periodic resonance responses are transited to the chaotic responses through the jump phenomenon.

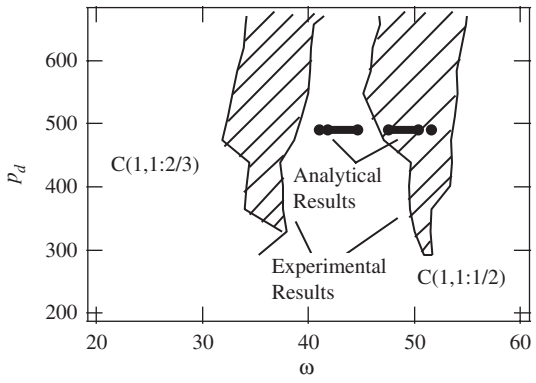


Fig. 8. Instability boundaries of the chaotic responses.

For the large amplitude response of the principal resonance (1,1:1), quantitative difference appears between the experiment and the analysis. The amplitude of response of the experiment is greater than that of the analysis at a same frequency. Large amplitude responses of the sub-harmonic resonance are shifted to the lower frequency range. The difference is due to the following reason. In the analysis, the restoring force of a softening-and-hardening spring is estimated as the strong hardening nonlinearity in the large deformation. And the simply supported boundary condition requires that the deflection at the edges of the shell-panel is zero. However, the edges of the shell-panel by the experiment seem to be elastically supported for deflection.

Changing the exciting amplitude $p_d$, instability boundaries of the chaotic responses are obtained by the experiment as shown in Fig. 8. The ordinate indicates the non-dimensional exciting amplitude $p_d$, while the abscissa presents the exciting frequency $\omega$. When the exciting amplitude $p_d$ is small, chaotic response is not generated. As the amplitude $p_d$ increases close to $p_d = 300$, both the chaotic responses of the types C(1,1:2/3) and C(1,1:1/2) are induced. When the amplitude $p_d$ is greater than the $p_d = 450$, both chaotic regions gradually spread to the wide range of frequency. As the exciting amplitude $p_d$ increases, the chaotic regions shift slightly to the higher frequency with the same width of instability range.

The frequency ranges of the chaotic responses obtained by the analysis are also shown by the solid circle under $p_d = 490$. Comparing the frequency ranges of the experiment and of the analysis under $p_d = 490$, the ranges both of the chaotic responses C(1,1:1/2) coincide well with each other. The chaotic response of C(1,1:2/3) of the experiment is located in the lower frequency range than the response of the analysis. Because the peak amplitude of the chaotic response is larger in the experiment than that in the analysis, frequency range of the chaotic response is also shifted to the lower range.

### 6.3. *Time histories and frequency spectra of chaotic responses*

Under the excitation amplitude $p_d = 490$, time histories and frequency spectra in the region of the chaotic response C(1,1:1/2) are obtained by the experiment and the analysis. The responses are measured at the position $\xi = 0.6$ and $\eta = 0.6$. Typical experimental results are shown in Fig. 9. In the figures of left side, the time histories of the deflection $\tilde{w}$ are shown with the time ratio $\tau/\tau_e$ normalized by the excitation period $\tau_e = 2\pi/\omega$. In the figures, the peak amplitude of the chaotic response shows irregular movement especially to negative $z$-direction. This irregular movement is due to the dynamic snap-through transition of the shell-panel. The figures of right-hand side show the Fourier spectra of the dominant chaotic responses. The abscissa indicates the non-dimensional Fourier frequency $\omega_{sp}$, while the ordinate denotes the amplitude $A$ of the spectrum scaled by decibel.

As can be seen in Fig. 9(a), Fourier spectrum at the frequency $\omega = 53.2$ has many spikes of spectrum distributed in wide range of Fourier frequency. The chaotic response involves many harmonic components. However, distinguished peak spectrum of the response can be detected at the half of exciting frequency $\omega$.

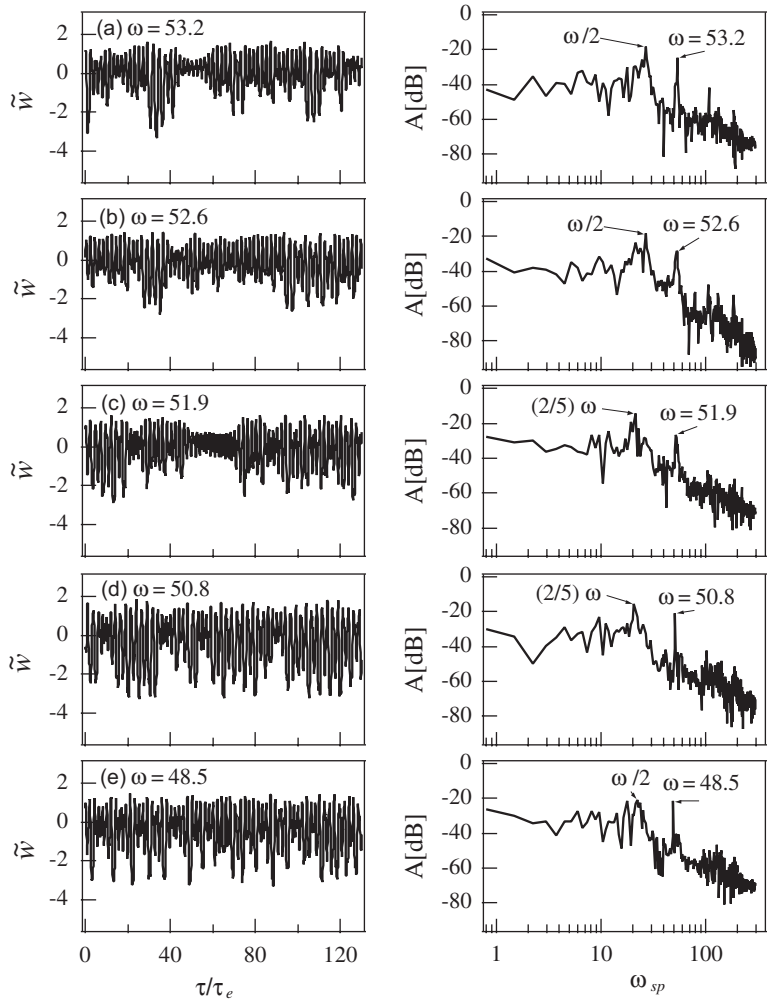


Fig. 9. Time histories and frequency spectra of the chaotic responses C(1,1:1/2), experimental results: (a) $\omega = 53.2$; (b) $\omega = 52.6$; (c) $\omega = 51.9$; (d) $\omega = 50.8$; (e) $\omega = 48.5$.

Therefore, the chaotic response C(1,1:1/2) is generated predominantly from the sub-harmonic response of $\frac{1}{2}$ order [25–27]. As the exciting frequency is decreased from $\omega = 53.2$, the chaotic response of the same type C(1,1:1/2) prevails to the frequency $\omega = 52.6$ as shown in Fig. 9(b). At the frequency $\omega = 51.9$ and at $\omega = 50.8$, chaotic response with large amplitude is prevailed, while the small amplitude response appears in short duration as shown in Figs. 9(c) and (d). In the figure of frequency spectrum, distinguished peak component appears at the frequency of $\frac{2}{5}$ of the exciting frequency. The spectrum is slightly deviated from the peak spectrum $(\frac{1}{2})\omega$ in Fig. 9(b). When the exciting frequency is $\omega = 48.5$ in Fig. 9(e), the chaotic response involves harmonic component of $\frac{1}{2}$ order.

Fig. 10 shows the time histories and corresponding frequency spectra obtained by the analysis in the region of the chaotic response C(1,1:1/2). In the numerical integrations of the Runge–Kutta–Gill method, time-step increment $\Delta\tau$ is chosen as $\frac{1}{240}$ of the exciting period $\tau_e$. After an initial transient response, which is caused by the numerical integration, is well damped, the result of response after $3700\tau_e$ is used for inspection of chaotic responses. In Fig. 10(a), the chaotic response includes the predominant component of the sub-harmonic resonance response of $\frac{1}{2}$ order in the Fourier spectrum at higher exciting frequency $\omega = 48.7$. As the exciting frequency is decreased, from $\omega = 48.3$ to 48.0 in Figs. 10(b) and (c), the Fourier spectrum of the chaotic responses C(1,1:1/2)

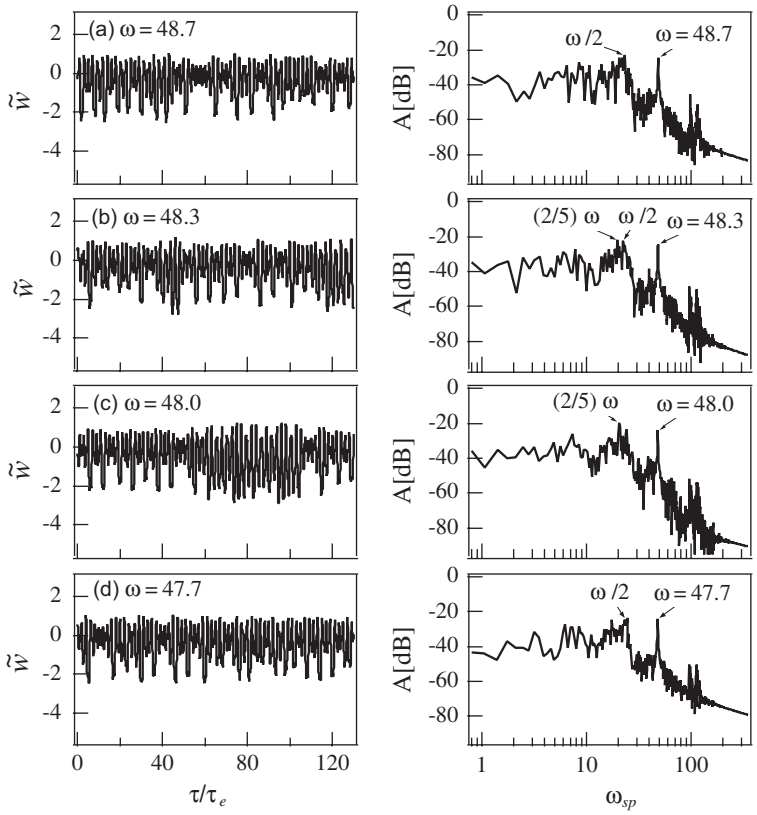


Fig. 10. Time histories and frequency spectra of the chaotic responses C(1,1:1/2), analytical results: (a) $\omega = 48.7$; (b) $\omega = 48.3$; (c) $\omega = 48.0$; (d) $\omega = 47.7$.

involve the harmonic components of $\frac{2}{5}$ of the exciting frequency. Furthermore, at the frequency $\omega = 47.7$, the predominant component of $\frac{1}{2}$ of the exciting frequency appears again in the chaotic response. According to the decrement of the exciting frequency, the large amplitude of time histories appears more frequently. Consequently, in the specific region of the frequency, the chaotic response C(1,1:1/2) has the harmonic component of the $\frac{2}{5}$ as well as the component of $\frac{1}{2}$ of the exciting frequency both in the experiment and in the analysis.

The other chaotic responses C(1,1:2/3) in the experiment are detected in the lower frequency range from $\omega = 39.4$ to 33.4 and are shown in Fig. 11. In Fig. 11(a) at the higher frequency $\omega = 39.4$, the chaotic response is generated close to the large amplitude response of the sub-harmonic resonance (1,1:1/2). When the exciting frequency is decreased to $\omega = 38.3, 37.1$ and 36.2, in Figs. 11(b)–(d), distinguished spectrum component of the chaotic response clearly appears at $\frac{2}{3}$ of the exciting frequency. This type of chaotic responses is closely related to the ultra-sub-harmonic resonance of $\frac{2}{3}$ order. In the lower range of the frequency $\omega = 33.4$, peaks of the spectrum are observed at the frequencies $(\frac{1}{2})\omega$ and $(\frac{2}{3})\omega$ simultaneously.

In the analysis, predominant chaotic responses C(1,1:2/3) are generated from the exciting frequency $\omega =$ 44.6 to 41.0. Fig. 12 shows the time histories and the corresponding Fourier spectra of C(1,1:2/3). In Fig. 12(a) at $\omega = 43.0$, the time history shows the large amplitude responses. As shown in the frequency response curves of Fig. 7(b), the amplitude covers the amplitudes of the sub-harmonic resonance (1,1:1/2) and the ultra-sub-harmonic resonance (1,1:2/3). It is found that the harmonic component of $\frac{2}{3}$ of the exciting frequency in the chaotic response C(1,1:2/3) is gradually increased in the decreased exciting frequency from $\omega = 43.0$ to 41.8.

In the Fourier spectrum of the chaotic time response, many spikes of the spectrum have been observed related to the resonance responses of the sub-harmonic resonance of order $\frac{1}{2}$ and the ultra-sub-harmonic resonance of order $\frac{2}{3}$. It can be explained that the chaotic responses are generated owing to the quadratic and the cubic nonlinear restoring force of the cylindrical shell-panel.

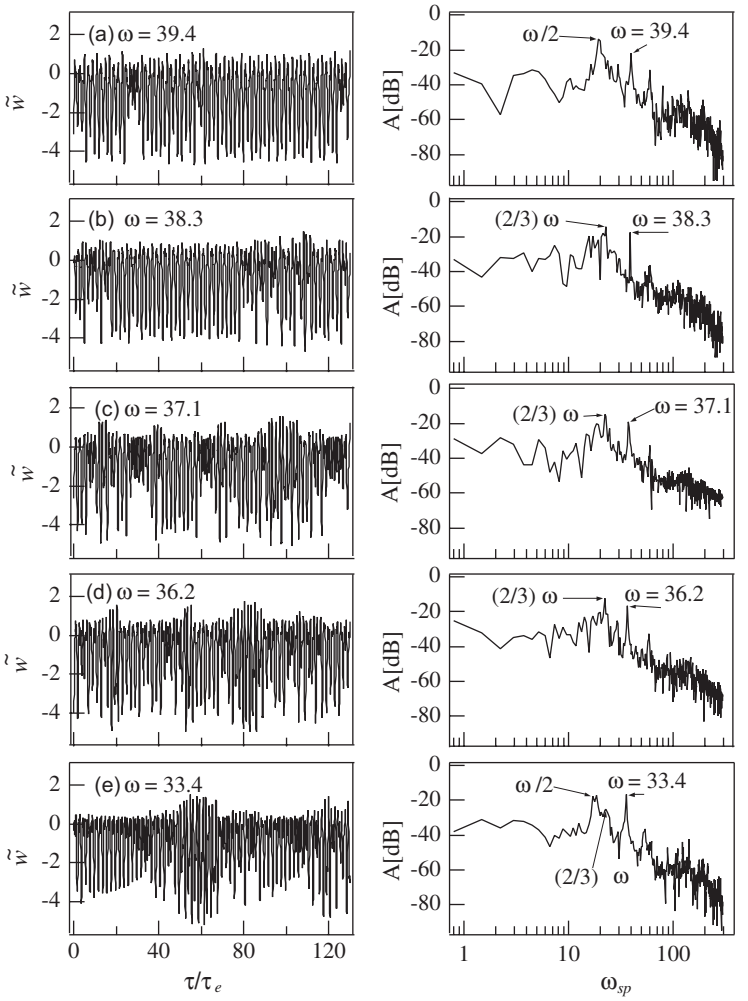


Fig. 11. Time histories and frequency spectra of the chaotic responses C(1,1:2/3), experimental results: (a) $\omega = 39.4$; (b) $\omega = 38.3$; (c) $\omega = 37.1$; (d) $\omega = 36.2$; (e) $\omega = 33.4$.

### 6.4. Poincaré projections of the shell-panel

In the experiment, the responses of the deflection $\tilde{w}$ and the velocity $\tilde{w}_{,\omega\tau}$ of the chaotic vibration are recorded at the position $\xi = 0.6, \eta = 0.6$ of the shell-panel. Fig. 13 shows the Poincaré projection of the chaotic response C(1,1:1/2). In each projection, 6000 points are plotted at the phase delay $\theta = \pi/2$ radian from the maximum amplitude of the exciting acceleration. In Figs. 13(a) and (b), the Poincaré projections at the frequency $\omega = 53.2$ and 52.6 have comparatively clear chaotic attractors and show a distinct fractal pattern with sharp bend. Decreasing the exciting frequency as shown in Figs. 13(c) and (d), the figures of the projections are gradually enlarged and the fractal patterns become more complicated ones. Furthermore, at $\omega = 50.4$ and 48.5 as shown in Figs. 13(e) and (f), the fractal patterns can be observed more clearly.

Fig. 14 shows the Poincaré projection of the chaotic response C(1,1:1/2) by changing the phase delay $\theta$. Fig. 14(a), in the left side, represents the experimental results, while Fig. 14(b) shows the analytical results. As the phase angle $\theta$ is shifted with $\pi/6$ radian, the attractor rotates clockwise. It is found that both projections of the experiment and the analysis closely resemble each other in the figure and the rotation in each phase angle.

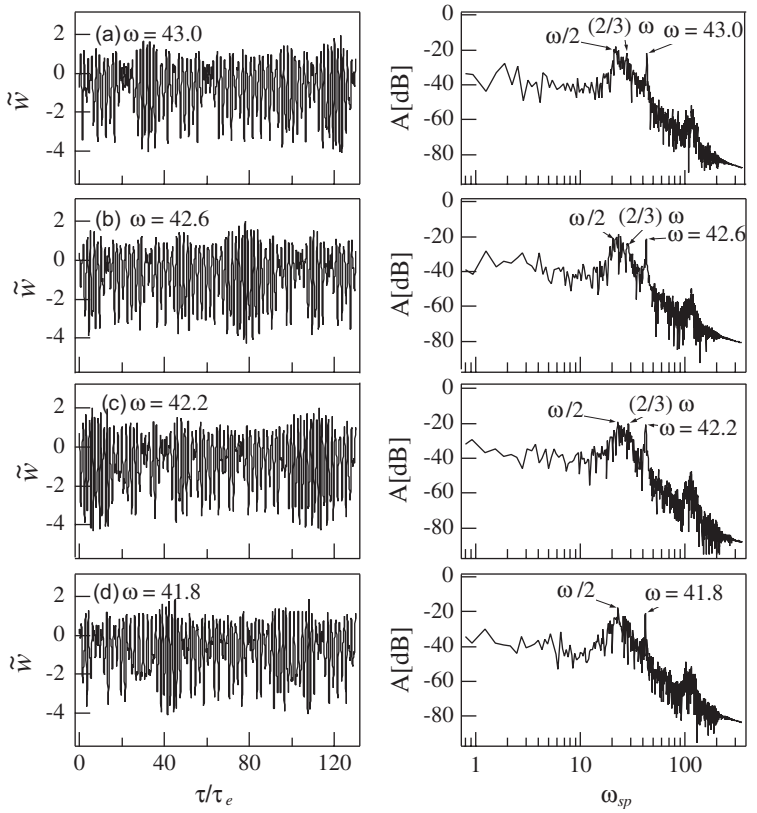


Fig. 12. Time histories and frequency spectra of the chaotic responses C(1,1:2/3), analytical results: (a) $\omega = 43.0$; (b) $\omega = 42.6$; (c) $\omega = 42.2$; (d) $\omega = 41.8$.

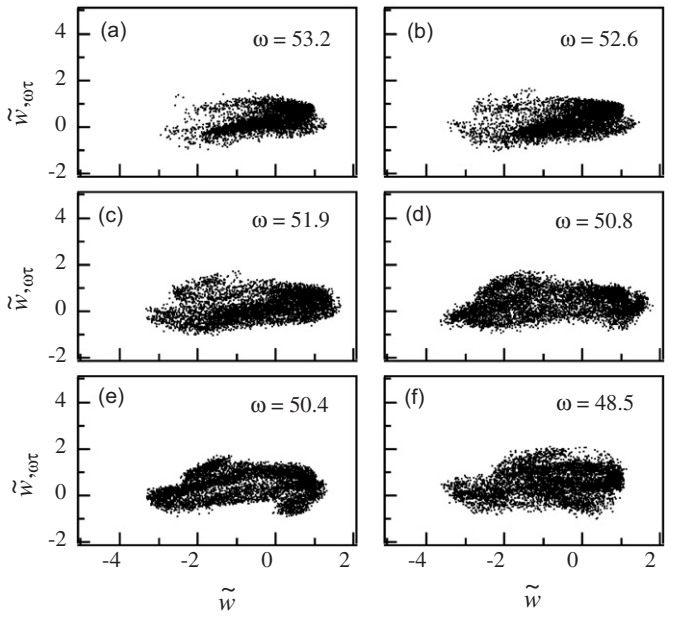


Fig. 13. Poincaré projections of the chaotic responses C(1,1:1/2), experimental results: (a) $\omega = 53.2$; (b) $\omega = 52.6$; (c) $\omega = 51.9$; (d) $\omega = 50.8$; (e) $\omega = 50.4$; (f) $\omega = 48.5$.

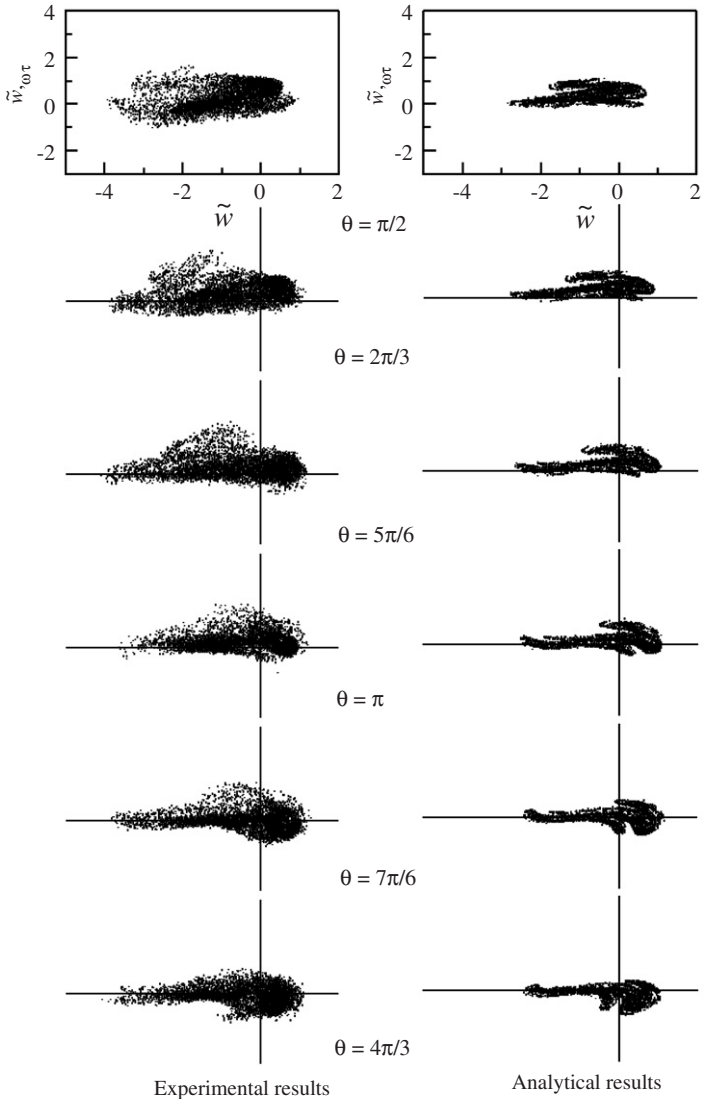


Fig. 14. Poincaré projections of the chaotic response C(1,1:1/2): (a) experimental results, $\omega = 52.6$; (b) analytical results, $\omega = 48.7$.

The Poincaré projections of the chaos C(1,1:2/3) in the experiment are shown in Fig. 15. The fractal patterns are different qualitatively from that of the chaos C(1,1:1/2) in Fig. 13. In Fig. 15(a) at the frequency $\omega = 39.4$, the Poincaré projection is separated into two groups. This projection represents the chaotic response close to the periodic response of the sub-harmonic resonance of $\frac{1}{2}$ order. When the frequency is decreased to $\omega = 39.2$ in Fig. 15(b), these two groups of projection are combined to a continuous figure. Furthermore, decreasing the exciting frequency from $\omega = 38.3$ to 36.2 as shown from Figs. 15(c)–(e), the Poincaré projections of the chaos C(1,1:2/3) show more complicated figure and clear fractal pattern on the phase plane. Finally at the frequency $\omega = 33.4$ in Fig. 15(f), the figure of Poincaré projection is focused to a condensed group locally compared with the figure in Fig. 15(e).

Fig. 16 shows the Poincaré projections of the chaos C(1,1:2/3) by the experiment and by the analysis with different phase delays. Both Poincaré projections show same fractal pattern clearly. Drastic changes of the Poincaré projections are also found in every change of the phase angle. The Poincaré projections of the chaos C(1,1:2/3) by the experiment coincide fairly well with the projections by the analysis.

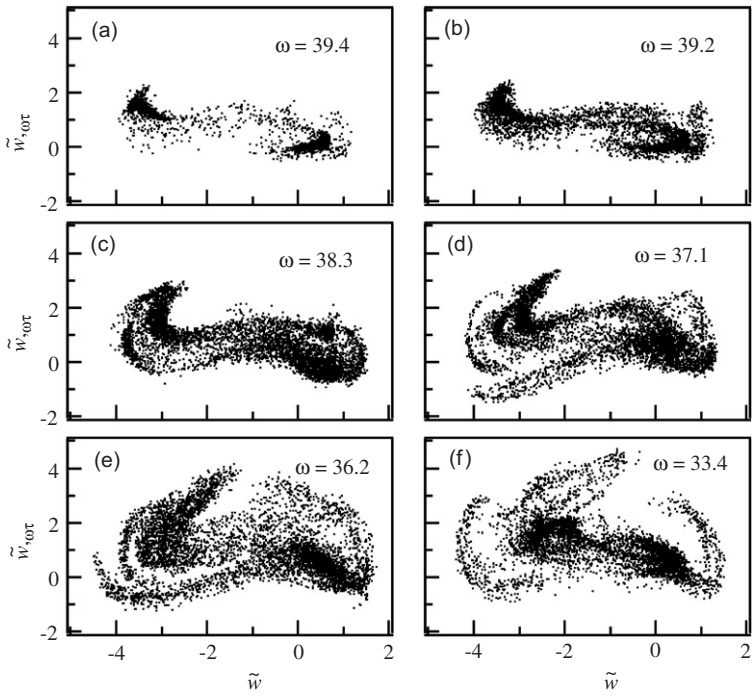


Fig. 15. Poincaré projections of the chaotic responses C(1,1:2/3), experimental results: (a) $\omega = 39.4$; (b) $\omega = 39.2$; (c) $\omega = 38.3$; (d) $\omega = 37.1$; (e) $\omega = 36.2$; (f) $\omega = 33.4$.

### 6.5. *The maximum Lyapunov exponents of the shell*

The maximum Lyapunov exponents of the chaotic response of the shell-panel are calculated, following the procedure by Wolf et al. [37] in Section 5, with our programming code. In the experimental results in Fig. 17(a), the maximum Lyapunov exponents have positive values in the frequency region of the chaotic responses. The responses are confirmed as the chaos. The exponents of the chaos C(1,1:1/2) take close values from $\lambda_{\max} = 1.9$ to 2.3, and averaged value is $\lambda_{\max} = 2.0$. In the region of the chaos C(1,1:2/3), the maximum Lyapunov exponents take smaller values than that of C(1,1:1/2). The maximum Lyapunov exponent ranges from $\lambda_{\max} = 0.9$ to 1.9, and averaged exponent takes $\lambda_{\max} = 1.7$.

Fig. 17(b) shows the maximum Lyapunov exponent $\lambda_{\max}$ calculated by the analysis. In the both regions of the chaotic responses C(1,1:1/2) and C(1,1:2/3), the positive Lyapunov exponents are obtained. The maximum Lyapunov exponents of the chaos C(1,1:1/2) take the averaged value $\lambda_{\max} = 2.5$. While, the maximum exponents of the chaos C(1,1:2/3) take the averaged value $\lambda_{\max} = 2.8$.

In the region of the chaos C(1,1:1/2), the maximum Lyapunov exponent $\lambda_{\max} = 2.0$ in the experiment agrees fairly well with the exponent $\lambda_{\max} = 2.5$ in the analysis. For the chaos C(1,1:2/3), the maximum Lyapunov exponent $\lambda_{\max} = 1.7$ in the experiment has a same order with the exponent $\lambda_{\max} = 2.8$ in the analysis. There is still small discrepancy between them, which remains to a future study on the shallow shell-panel.

Fig. 18(a) shows the maximum Lyapunov exponents $\lambda_{\max}$ related to the embedding dimension $e$ in the chaotic region of C(1,1:1/2) obtained by the experiment. As the embedding dimension increases more than $e = 6$, the maximum Lyapunov exponents $\lambda_{\max}$ converge to a positive constant value. In the analysis, the Lyapunov dimension $d_L$ of the chaotic response C(1,1:1/2) is calculated by changing the assumed number of vibration modes $I_c$. The result of the Lyapunov dimensions, which is averaged in the region of the chaos, is shown in Fig. 18(b). When the number of modes $I_c$ is increased close to $I_c = 3$ and 4, the Lyapunov dimension $d_L$ converges to the value $d_L = 5.7$. Consequently, the number of predominant modes of vibration generated in the chaos C(1,1:1/2) is counted as three.

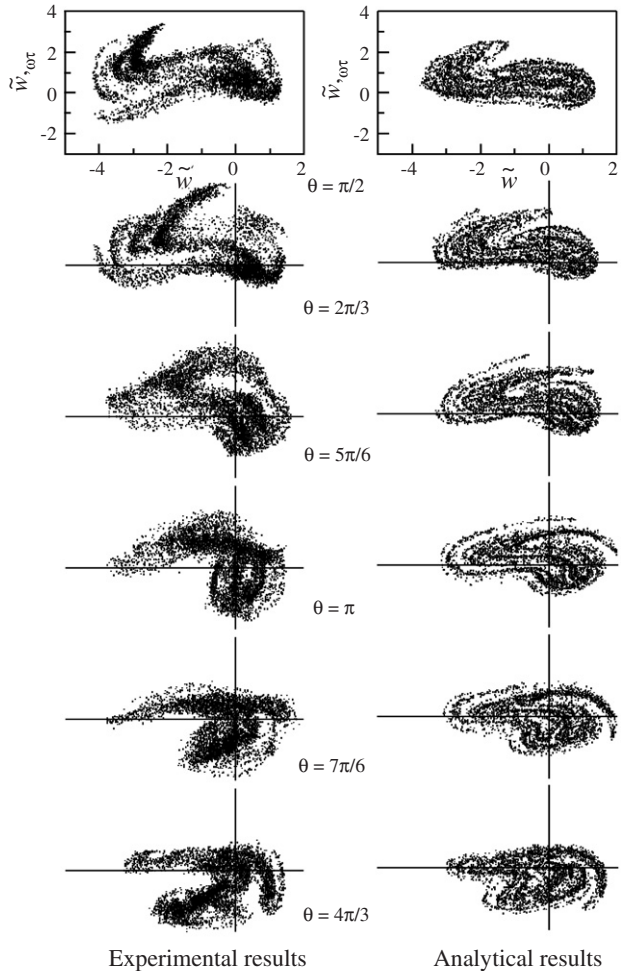


Fig. 16. Poincaré projections of the chaotic response C(1,1:2/3): (a) experimental results, $\omega = 37.1$; (b) analytical results, $\omega = 42.6$.

For the chaotic response C(1,1:2/3), the convergence of the maximum Lyapunov exponent in the experiment and the Lyapunov dimension in the analysis is shown in Fig. 19. It is observed that the maximum Lyapunov exponents $\lambda_{\max}$ converge to positive magnitudes within the embedding dimension $e = 7$ and 8 in Fig. 19(a), while the Lyapunov dimension saturates to $d_L = 6.7$ with the number of mode $I_c = 4$ in Fig. 19(b). Therefore, four modes of vibration are generated predominantly in the chaotic response C(1,1:2/3).

## 7. Conclusions

Precise experimental results and analytical results have been presented on chaotic vibrations of a shallow cylindrical shell-panel with simply supported edges subjected to the gravity and periodic acceleration. Main results are summarized as follows.

(1) Two types of chaotic vibrations are bifurcated predominantly from the sub-harmonic resonance response of $\frac{1}{2}$ order and the ultra-sub-harmonic resonance response of $\frac{2}{3}$ order, corresponding to the lowest mode of vibration. The chaotic responses are induced owing to the quadratic and cubic nonlinear restoring forces.

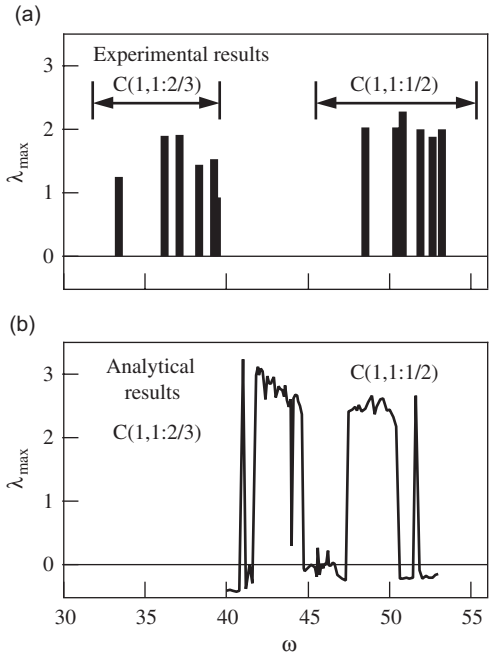


Fig. 17. Maximum Lyapunov exponent related to exciting frequency: (a) experimental results; (b) analytical results.

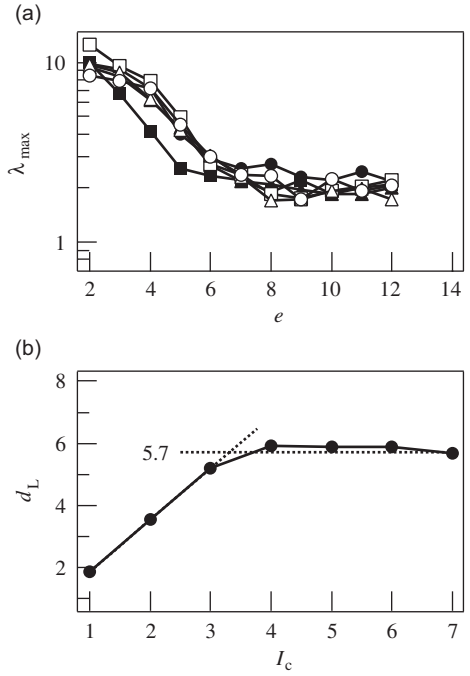


Fig. 18. Maximum Lyapunov exponents and Lyapunov dimension, C(1,1:1/2): (a) experimental results of maximum Lyapunov exponent, ◯ $\omega = 53.2$, △ $\omega = 52.6$, □ $\omega = 51.9$, • $\omega = 50.8$, ▲ $\omega = 50.4$, ■ $\omega = 48.5$; (b) analytical results of Lyapunov dimension, averaged value in C(1,1:1/2).

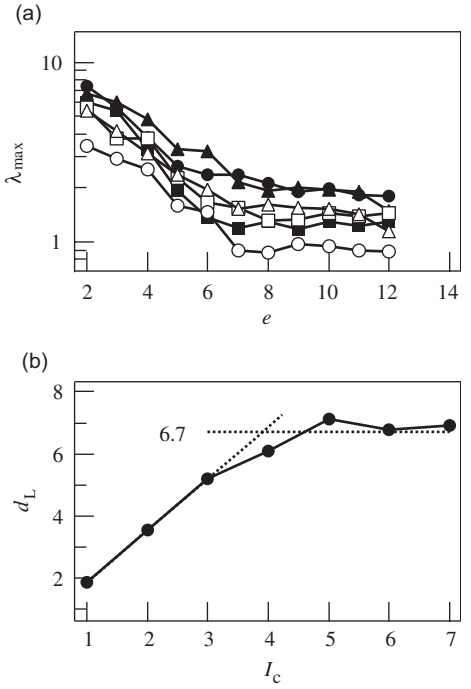


Fig. 19. Maximum Lyapunov exponents and Lyapunov dimension, C(1,1:2/3): (a) experimental results of maximum Lyapunov exponent, ◯ $\omega = 39.4$, △ $\omega = 39.2$, □ $\omega = 38.3$, • $\omega = 37.1$, ▲ $\omega = 36.2$, ■ $\omega = 33.4$; (b) analytical results of Lyapunov dimension, averaged value in C(1,1:2/3).

The responses are accompanied with the dynamic snap-through which is originated by the restoring force of the softening-and-hardening type including negative gradient.

(2) When the exciting frequency decreases in the experiment, the two types of chaotic responses are bifurcated continuously from the periodic response of the sub-harmonic resonance of order $\frac{1}{2}$. As the frequency increases, chaotic response is suddenly generated by the transition from the large amplitude principal resonance and from the non-resonant response through the jump phenomenon.

(3) The Poincaré projection of the chaos related to the sub-harmonic response of $\frac{1}{2}$ order has qualitative difference with the projection of the chaos of the ultra-sub-harmonic response of $\frac{2}{3}$ order. The fairly good agreements are obtained in the Poincaré projections of the chaos in the experiment and in the analysis.

(4) The maximum Lyapunov exponents of the two types of the chaotic responses take the same order around $\lambda_{max} = 2$ in the experiment and in the analysis. In the experiment, three modes of vibration contribute to the chaotic response bifurcated from the sub-harmonic resonance of order $\frac{1}{2}$. While, the chaos bifurcated from the ultra-sub-harmonic resonance of order $\frac{2}{3}$ involves four modes of vibration. The same features are also confirmed with the Lyapunov dimension in the analysis.

## Acknowledgments

The authors show profound thanks to Mr. Takayuki Hata (Anesto Iwata Corporation), Mr. Dai Yanagisawa (Mitsuba Corporation) and Mr. Mitsuru Oya (Tobu Railways Co., Ltd.) for their great assistance in the experiment and the calculation.

## Appendix A

The coefficients in Eq. (10) are shown below in the solution of the compatibility equation (1):

$$
\begin{aligned}
d_{mn}^{(0)} &= c(\alpha_y\overline{m}^2+\alpha_x\beta^2\overline{n}^2)/(\overline{m}^2+\beta^2\overline{n}^2)^2,\\
\theta_{klmn}^{(1)} &= -(c\beta^2/8)(\overline{m}\overline{l}-\overline{k}\overline{n})^2(1-\delta_{km})(1-\delta_{ln})/\{(\overline{k}-\overline{m})^2+\beta^2(\overline{l}-\overline{n})^2\}^2,\\
\theta_{klmn}^{(2)} &= (c\beta^2/8)(\overline{m}\overline{l}+\overline{k}\overline{n})^2/\{(\overline{k}-\overline{m})^2+\beta^2(\overline{l}+\overline{n})^2\}^2,\\
\theta_{klmn}^{(3)} &= (c\beta^2/8)(\overline{m}\overline{l}+\overline{k}\overline{n})^2/\{(\overline{k}+\overline{m})^2+\beta^2(\overline{l}-\overline{n})^2\}^2,\\
\theta_{klmn}^{(4)} &= -(c\beta^2/8)(\overline{m}\overline{l}-\overline{k}\overline{n})^2/\{(\overline{k}+\overline{m})^2+\beta^2(\overline{l}+\overline{n})^2\}^2,
\end{aligned}
$$

where the symbol $\delta_{km}$ is the Kronecker's delta.

## Appendix B

The coefficients are shown below related to the in-plane elastic support in Eq. (11):

$$
\begin{aligned}
d_{mn}^{(1)} &= k_0\{K_{mn}^{(1)}/c_x+\nu K_{mn}^{(2)}/c\}\Pi_m\Pi_n,\\
d_{mn}^{(2)} &= (k_0/\beta^2)\{K_{mn}^{(2)}/c_y+\nu K_{mn}^{(1)}/c\}\Pi_m\Pi_n,\\
\Pi_m &\equiv [(-1)^m-1](1-\delta_{m0})/\overline{m},\\
e_{mn}^{(1)} &= -(k_0/8)(K_{mn}^{(3)}/c_x+\nu K_{mn}^{(4)}/c),\\
e_{mn}^{(2)} &= -k_0/(8\beta^2)(K_{mn}^{(4)}/c_y+\nu K_{mn}^{(3)}/c),\\
g_1 &= k_0\{\beta(v_0-v_b)/c_x+\nu(u_0-u_a)/c\},\\
g_2 &= (k_0/\beta^2)\{(u_0-u_a)/c_y+\nu\beta(v_0-v_b)/c\},\\
1/c_x &= 2/k_x+1/c,\\
1/c_y &= 2\beta/k_y+1/c,\\
k_0 &= -\{1/(c_xc_y)-\nu^2/c^2\}^{-1},\\
K_{mn}^{(1)} &= d_{mn}^{(0)}(-\overline{m}^2+\nu\beta^2\overline{n}^2)/c+\alpha_y,\\
K_{mn}^{(2)} &= d_{mn}^{(0)}(-\beta^2\overline{n}^2+\nu\overline{m}^2)/c+\alpha_x,\\
K_{mn}^{(3)} &= \beta^2\overline{n}^2+\nu\overline{m}^2,\\
K_{mn}^{(4)} &= \nu\beta^2\overline{n}^2+\overline{m}^2.
\end{aligned}
$$

## Appendix C

The coefficients are shown below in the nonlinear ordinary differential equation Eq. (13):

$$\hat{B}_{rsmn} \equiv (\tfrac{1}{4})\delta_{rm}\delta_{sn},$$

$$\hat{C}_{rsmn} \equiv (\tfrac{1}{4})\{(\overline{m}^2+\beta^2\overline{n}^2)^2+d_{mn}^{(0)}(\alpha_x\beta^2\overline{n}^2+\alpha_y\overline{m}^2)+\beta^2(g_2\overline{m}^2+g_1\overline{n}^2)\}\delta_{rm}\delta_{sn}-(\alpha_x\beta^2d_{mn}^{(2)}+\alpha_yd_{mn}^{(1)})\Pi_r\Pi_s,$$

$$
\begin{aligned}
\hat{D}_{rsklmn} \equiv\ & -\alpha_x\beta^2(\Theta_{rsklmn}^{(1)}+e_{mn}^{(2)}\delta_{mk}\delta_{nl}\Pi_r\Pi_s)\\
& -\alpha_y(\Theta_{rsklmn}^{(2)}+e_{mn}^{(1)}\delta_{mk}\delta_{nl}\Pi_r\Pi_s)\\
& +\beta^2[d_{mn}^{(0)}\{(\tfrac{1}{8})J_{rsklmn}^{(+)}-(\overline{k}^2\overline{n}^2+\overline{l}^2\overline{m}^2)J_{rsklmn}^{(-)}\}\\
& +(\tfrac{1}{4})\delta_{rk}\delta_{sl}(d_{mn}^{(2)}\overline{k}^2+d_{mn}^{(1)}\overline{l}^2)],
\end{aligned}
$$

$$\begin{aligned}
\hat{E}_{rsmnklij} &\equiv \beta^2\{\bar{i}^2 K^{(1)}_{rsmnklij} + \bar{j}^2 K^{(2)}_{rsmnklij} + 2\bar{i}\,\bar{j} K^{(3)}_{rsmnklij} \\
&\quad + (\tfrac{1}{4})\delta_{mk}\delta_{nl}\delta_{ri}\delta_{sj}(e^{(2)}_{mn}\bar{i}^2 + e^{(1)}_{mn}\bar{j}^2)\}, \\
\hat{F}_{rs} &\equiv -(\alpha_x\beta^2 g_2 + \alpha_y g_1)\Pi_r\Pi_s, \\
\hat{G}_{rs} &\equiv \Pi_r\Pi_s,
\end{aligned}$$

$$\begin{aligned}
\Theta^{(1)}_{rsklmn} &\equiv -(\tfrac{1}{4})[(\bar{l}-\overline{n})^2(\Pi_{l-n-s} - \Pi_{l-n+s}) \\
&\quad \times\{\theta^{(1)}_{klmn}(\Pi_{k-m-r} - \Pi_{k-m+r}) + \theta^{(3)}_{klmn}(\Pi_{k+m-r} - \Pi_{k+m+r})\} \\
&\quad + (\bar{l}+\overline{n})^2(\Pi_{l+n-s} - \Pi_{l+n+s}) \\
&\quad \times\{\theta^{(2)}_{klmn}(\Pi_{k-m-r} - \Pi_{k-m+r}) + \theta^{(4)}_{klmn}(\Pi_{k+m-r} - \Pi_{k+m+r})\}], \\
\Theta^{(2)}_{rsklmn} &\equiv -(\tfrac{1}{4})[(\overline{k}-\overline{m})^2(\Pi_{k-m-r} - \Pi_{k-m+r}) \\
&\quad \times\{\theta^{(1)}_{klmn}(\Pi_{l-n-s} - \Pi_{l-n+s}) + \theta^{(2)}_{klmn}(\Pi_{l+n-s} - \Pi_{l+n+s})\} \\
&\quad + (\overline{k}+\overline{m})^2(\Pi_{k+m-r} - \Pi_{k+m+r}) \\
&\quad \times\{\theta^{(3)}_{klmn}(\Pi_{l-n-s} - \Pi_{l-n+s}) + \theta^{(4)}_{klmn}(\Pi_{l+n-s} - \Pi_{l+n+s})\}], \\
J^{(-)}_{rsmnkl} &= (\tfrac{1}{16})[(\Pi_{k-m-r} - \Pi_{k-m+r}) - (\Pi_{k+m-r} - \Pi_{k+m+r})] \\
&\quad \times[(\Pi_{l-n-s} - \Pi_{l-n+s}) - (\Pi_{l+n-s} - \Pi_{l+n+s})], \\
J^{(+)}_{rsmnkl} &= [(\Pi_{k-m-r} - \Pi_{k-m+r}) + (\Pi_{k+m-r} - \Pi_{k+m+r})] \\
&\quad \times[(\Pi_{l-n-s} - \Pi_{l-n+s}) + (\Pi_{l+n-s} - \Pi_{l+n+s})], \\
\Delta_{ijk} &= (\tfrac{1}{4})[\delta_{(i-j-k),0} - \delta_{(i-j+k),0} - \delta_{(i+j-k),0} - \delta_{(i+j+k),0}], \\
K^{(1)}_{rsmnklij} &= -(\theta^{(1)}_{klmn}\Delta_{r(k-m)i} + \theta^{(3)}_{klmn}\Delta_{r(k+m)i})(\bar{l}-\overline{n})^2\Delta_{s(l-n)j} \\
&\quad - (\theta^{(2)}_{klmn}\Delta_{r(k-m)i} + \theta^{(4)}_{klmn}\Delta_{r(k+m)i})(\bar{l}+\overline{n})^2\Delta_{s(l+n)j}, \\
K^{(2)}_{rsmnklij} &= -[\theta^{(1)}_{klmn}(\overline{k}-\overline{m})^2\Delta_{r(k-m)i} + \theta^{(3)}_{klmn}(\overline{k}+\overline{m})^2\Delta_{r(k+m)i}]\Delta_{s(l-n)j} \\
&\quad - [\theta^{(2)}_{klmn}(\overline{k}-\overline{m})^2\Delta_{r(k-m)i} + \theta^{(4)}_{klmn}(\overline{k}+\overline{m})^2\Delta_{r(k+m)i}]\Delta_{s(l+n)j}, \\
K^{(3)}_{rsmnklij} &= [\theta^{(1)}_{klmn}(\overline{k}-\overline{m})^2\Delta_{ri(k-m)} + \theta^{(3)}_{klmn}(\overline{k}+\overline{m})\Delta_{ri(k+m)}](\bar{l}-\overline{n})\Delta_{sj(l-n)} \\
&\quad + [\theta^{(2)}_{klmn}(\overline{k}-\overline{m})\Delta_{ri(k-m)} + \theta^{(4)}_{klmn}(\overline{k}+\overline{m})\Delta_{ri(k+m)}](\bar{l}+\overline{n})\Delta_{sj(l+n)}.
\end{aligned}$$

## References


[1] D.A. Evensen, Some observations on the non-linear vibration of thin cylindrical shells, *American Institute of Aeronautics and Astronautics Journal* 1 (1963) 2857–2858.

[2] D.A. Evensen, Nonlinear flexural vibrations of thin circular rings, *Transaction of the ASME, Ser E, Journal of Applied Mechanics* 33 (1966) 553–560.

[3] M.D. Olson, Some experimental observations on the nonlinear vibration of cylindrical shells, *American Institute of Aeronautics and Astronautics Journal* 3 (1965) 1775–1777.

[4] Y. Matsuzaki, S. Kobayashi, A theoretical and experimental study on the nonlinear flexural vibration of thin circular cylindrical shell with clamped ends, *Transaction of the Japanese Society for Aeronautics and Space Sciences* 12 (1969) 55–62.

[5] J.C. Chen, C.D. Babcock, Nonlinear vibration of cylindrical shells, *American Institute of Aeronautics and Astronautics Journal* 13 (1975) 868–876.

[6] M. Chiba, Non-linear hydroelastic vibration of a cantilever cylindrical tank—I. Experiment (empty case), *International Journal of Non-Linear Mechanics* 28 (1993) 591–599.

[7] F. Pellicano, M. Amabili, M.P. Païdoussis, Effect of the geometry on the non-linear vibration of circular cylindrical shells, *International Journal of Non-Linear Mechanics* 37 (2002) 1181–1198.

[8] M. Amabili, Theory and experiments for large-amplitude vibrations of empty and fluid-filled circular cylindrical shells with imperfections, *Journal of Sound and Vibration* 262 (2003) 921–975.

[9] Y. Kobayashi, A.W. Leissa, Large amplitude free vibration of thick shallow shells supported by shear diaphragms, *International Journal of Non-Linear Mechanics* 30 (1995) 57–66.
[10] M. Amabili, M. Pellegrini, M. Tommesani, Experiment on large-amplitude vibration of a circular cylindrical panel, *Journal of Sound and Vibration* 260 (2003) 537–547.
[11] E.H. Dowell, Flutter of a buckled plate as an example of chaotic motion of a deterministic autonomous systems, *Journal of Sound and Vibration* 85 (1982) 333–344.
[12] A.H. Nayfeh, R.A. Raouf, Nonlinear forced response of infinitely long circular shells, *Journal of Applied Mechanics* 54 (1987) 571–577.
[13] H.L. Yang, P.R. Sethna, Non-linear phenomena in forced vibrations of a nearly square plate, *Journal of Sound and Vibration* 155 (1992) 413–441.
[14] S.I. Chang, A.K. Bajaj, C.M. Krousgrill, Nonlinear vibrations and chaos in harmonically excited rectangular plates with one-to-one internal resonance, *Nonlinear Dynamics* 4 (1993) 433–460.
[15] J. Fan, F. He, Z. Liu, Chaotic oscillation of saddle form cable-suspended roofs under vertical excitation action, *Nonlinear Dynamics* 12 (1997) 57–68.
[16] A.A. Popov, J.M.T. Thompson, F.A. McRobie, Chaotic energy exchange through auto-parametric resonance in cylindrical shells, *Journal of Sound and Vibration* 248 (2001) 395–411.
[17] M.S. Soliman, P.B. Gonçalves, Chaotic behavior resulting in transient and steady state instabilities of pressure-loaded shallow spherical shells, *Journal of Sound and Vibration* 259 (2003) 497–512.
[18] M. Amabili, Non-linear vibrations of doubly curved shallow shells, *International Journal of Non-Linear Mechanics* 40 (2005) 683–710.
[19] R.C. Zhou, D.Y. Xue, C. Mei, Finite element time domain-modal formulation for nonlinear flutter of composite panels, *American Institute of Aeronautics and Astronautics Journal* 32 (1994) 2042–2052.
[20] C. Sansour, P. Wriggers, J. Sansour, Nonlinear dynamics of shells: theory, finite element formulation, and integration schemes, *Nonlinear Dynamics* 13 (1997) 279–305.
[21] L. Maestrello, A. Frendi, D.E. Brown, Nonlinear vibration and radiation from a panel with transition to chaos, *American Institute of Aeronautics and Astronautics Journal* 30 (1992) 2632–2638.
[22] K.D. Murphy, L.N. Virgin, S.A. Rizzi, Characterizing the dynamics response of a thermally loaded, acoustically excited plate, *Journal of Sound and Vibration* 196 (1996) 635–658.
[23] K. Nagai, Nonlinear vibrations of a shallow arch under periodic lateral force (theory), *Transaction of the Japan Society of Mechanical Engineers* 51 (1985) 2820–2827 (in Japanese).
[24] K. Nagai, Nonlinear vibrations of a shallow arch under periodic lateral force (2nd Report, Experiment), *Transaction of the Japan Society of Mechanical Engineers* 52 (1986) 3047–3054 (in Japanese).
[25] K. Nagai, Experimental study of chaotic vibration of a clamped beam subjected to periodic lateral forces, *Transaction of the Japan Society of Mechanical Engineers* 56 (1990) 1171–1177 (in Japanese).
[26] K. Nagai, T. Yamaguchi, Chaotic vibrations of a post-buckled beam carrying a concentrated mass (1st Report, Experiment), *Transaction of the Japan Society of Mechanical Engineers* 60 (1994) 3733–3740 (in Japanese).
[27] T. Yamaguchi, K. Nagai, Chaotic vibrations of a post- buckled beam carrying a concentrated mass (2nd Report, Theoretical Analysis), *Transaction of the Japan Society of Mechanical Engineers* 60 (1994) 3741–3748 (in Japanese).
[28] K. Nagai, K. Kasuga, M. Kamada, T. Yamaguchi, K. Tanifuji, Experiment on chaotic oscillations of a post-buckled reinforced beam constrained by an axial spring, *International Journal of the Japan Society of Mechanical Engineers* 41 (1998) 563–569.
[29] K. Nagai, S. Maruyama, K. Sakaimoto, T. Yamaguchi, Experiments on chaotic vibrations of a post-buckled beam with an axial elastic constraint, *Journal of Sound and Vibration* 304 (2007) 541–555.
[30] K. Nagai, T. Yamaguchi, Chaotic oscillations of a shallow cylindrical shell with rectangular boundary under cyclic excitation, *High Pressure Technology, ASME, PVP* 297 (1995) 107–115.
[31] T. Yamaguchi, K. Nagai, Chaotic vibration of a cylindrical shell-panel with an in-plane elastic-support at boundary, *Nonlinear Dynamics* 13 (1997) 259–277.
[32] K. Nagai, S. Maruyama, M. Oya, T. Yamaguchi, Chaotic oscillations of a shallow cylindrical shell with a concentrated mass under periodic excitation, *Computers and Structures* 82 (2004) 2607–2619.
[33] L.H. Donnell, Stability of thin-walled tubes under torsion, NACA Report 479, 1935, pp. 95–116.
[34] L.H. Donnell, *Beams, Plates and Shells*, McGraw-Hill, New York, 1976.
[35] C.S. Ventres, E.H. Dowell, Comparison of theory and experiment for nonlinear flutter of loaded plates, *American Institute of Aeronautics and Astronautics Journal* 8 (1970) 2022–2030.
[36] M. Urabe, A. Reiter, Numerical computation of nonlinear forced oscillations by Galerkin's procedure, *Journal of Mathematical Analysis and Applications* 14 (1966) 107–140.
[37] A. Wolf, J.B. Swift, H.L. Swinney, J.A. Vastano, Determining Lyapunov exponents from a time series, *Physica* 16D (1985) 285–317.
[38] J. Kaplan, J. Yorke, The Lyapunov dimension of strange attractors, *Journal of Differential Equations* 49 (1983) 185–207.
[39] C. Pezeshki, E.H. Dowell, Generation and analysis of Lyapunov exponents for the buckled beam, *International Journal of Non-Linear Mechanics* 24 (2) (1989) 79–97.
[40] F. Takens, Detecting strange attractors in turbulence, in: D. Rand, L. Young (Eds.), *Lecture Notes in Mathematics*, Vol. 898, Springer, New York, 1981, pp. 366–381.